On the Influence of Control Type and Strain Rate on the Lifetime of 50CrMo4

Max Benedikt Geilen[1]* [iD], Josef Arthur Schönherr[1] [iD], Marcus Klein[1] [iD], Dominik Sebastian Leininger[1] [iD], Alexander Giertler[2], Ulrich Krupp[3], Matthias Oechsner[1]

[1]   Centre for Engineering Materials (MPA-IfW); Technical University of Darmstadt; Grafenstraße 2 64283 Darmstadt, Germany; geilen@mpa-ifw.tu-darmstadt.de

[2]   Institute of Materials Design and Structural Integrity; Osnabrück University of Applied Sciences; Albrechtstraße 30 49009 Osnabrück; a.giertler@hs-osnabrueck.de

[3]   Steel Institute RWTH Aachen University; Intzestraße 1 52072 Aachen ; krupp@iehk.rwth-aachen.de

*   Correspondence: geilen@mpa-ifw.tu-darmstadt.de; Tel.: +49-6151-16-25867

Abstract: In this study, we investigate the influence of control type and strain rate on the lifetime of specimens manufactured from 50CrMo4. This influence is described by a strain rate dependent method that uses cyclic stress strain curves to correct displacement controlled cyclic test results. The objective of this correction is to eliminate the stress related differences between displacement controlled cyclic test results and force controlled cyclic test results. The method is applied to the results of ultrasonic fatigue tests of six different combinations of heat treatment, specimen geometry (notch factor) and atmosphere. In a statistical analysis, the corrected results show an improved agreement with test results obtained on conventional fatigue testing equipment with similar specimens: the standard deviation in combined data sets is significantly reduced (p=4.1%). We discuss the literature on intrinsic and extrinsic strain rate effects in carbon steels.

Keywords: ultrasonic cyclic testing, frequency effect, control type effect, strain rate effect, 50CrMo4, SAE 4150, High Cycle Fatigue, Very High Cycle Fatigue, statistical analyses

---

1. Introduction

Since the early days of fatigue research, stress based approaches have been used for the fatigue design of components. This approach prevails in the High Cycle Fatigue (HCF) region to this day. Models of this kind are best calibrated using stress controlled cyclic tests. In the 1950s and 1960s, strain-based approaches, which differentiate between elastic and plastic strain, were developed to improve predictive power in the Low Cycle Fatigue (LCF) region [1]. Strain-based models are best calibrated using strain controlled fatigue tests. In the 1980s and 1990s, component failures in the gigacycle range kick-started Very High Cycle Fatigue (VHCF) research [2–35]. In VHCF fatigue initiation, no macroscopically plastic material behavior is observed, therefore stress based models are employed. Ideally, these models should be calibrated using stress controlled cyclic tests.

Materials testing in the VHCF region is conducted on two kinds of fundamentally different testing setups. The first kind are conventional testing machines – e.g. resonance or servo-hydraulic testing machines – which are also used in the HCF region. These machines are able to operate under stress control but rarely exceed testing frequencies of 200 Hz[1], typical testing frequencies range from 20 to 100 Hz. The second kind is ultrasonic fatigue testing machines. They reach effective testing frequencies

---

[1]   Some state of the art testing machines like RUMUL GIGAFORTE 50 reach up to 1000 Hz.

of 2 kHz^2 but operate under displacement control [26]. In cyclically softening steel specimens under displacement control, notch stress amplitudes may decrease over the course of the cyclic test.

In research on low strength (ultimate tensile strength 919 MPa) cyclically softening 50CrMo4 [10], differences between the results of displacement controlled cyclic tests conducted at about 20 kHz and the results of force controlled cyclic tests conducted between 20 Hz and 700 Hz were observed. Such differences have largely been attributed to a frequency or strain rate effect [6,11,12,36–39]. In research on high strength (ultimate tensile strength 1726 MPa) 50CrMo4, the observed differences between such tests were remarkably smaller, which has been attributed to a lower strain rate influence for high strength steels [6]. The understanding of these test results without further processing is limited by the coupling between strain rate and control type.

In components testing, displacement controlled cyclic tests are conducted to simultaneously test dozens of specimens with a single testing machine [20], which allows testing much larger numbers of specimens at a given budget. These results should be used to design force loaded components only after correction for control type.

In this study, an algorithm [40] implementing a method for the strain rate dependent correction for control type [10] is utilized to create control type corrected cyclic test results from displacement controlled cyclic test results for different batches of 50CrMo4. We show that for each batch, these corrected results show an equal or improved agreement with results of force controlled cyclic tests in the HCF range.

In section 2, a brief overview on strain rate effects in fatigue is given. In section 3, the data used in this investigation is described. In section 4, the numerical methods of the investigation are described. In section 5, the results of the investigation are presented. In section 6, conclusions are drawn.

2. Effects of Strain Rate on Deformation and Fatigue

A multitude of studies on fatigue life were conducted at different strain rates on steels [6,36,39, 41–51] as well as other materials [41,52–62]. The results of these studies are mixed, some showing momentous differences in fatigue life, some showing ambiguous results implying there is no significant strain rate influence in these investigations. In this section, we describe different effects suspected to cause strain rate effects.

Frequency and strain rate effects may be divided into intrinsic effects and extrinsic effects [11]. Effects are called intrinsic if they are caused directly by strain rate dependent material behavior. An intrinsic effect at microscopic scale is a change in the formation process of slip bands or an activation of dynamic strain aging effects. These effects at microscopic scale cause effects at macroscopic scale, for example an increase in monotonic and cyclic yield strength. These effects are well studied for monotonic loading [63–71]. For cyclic loading, fewer studies are available [60,61,64,72]. Extrinsic effects are effects that sometimes or always accompany strain rate effects but are at least in theory separable from intrinsic strain rate effects. Important extrinsic effects are temperature, hydrogen and chlorine concentration in the crack tip due to diffusion, control type, testing volume and oxidation-induced crack closure.

2.1. Intrinsic Effects

Since cyclic deformation is the sum of a succession of monotonic deformations, it is natural to assume that qualitatively, the same effects apply for monotonic and cyclic deformations. Therefore, we first explain the much better studied monotonic effects on deformation behavior. While the strain rate

---

2   The tests run at 20 kHz but must be run in pulse pause mode because the specimen heats up. Depending on geometry, tolerated temperature increase, material under investigation, load level and cooling equipment, the effective testing frequency varies.

70 dependency is fundamentally different for some materials [73], we will focus on the description of the
71 state of research on carbon steels.

72   At microscopic scale, strain rate is closely linked to the activation energy of dislocations. For
73 dislocations to form or move, a certain energy must be supplied locally [69]. In a given material at
74 a given temperature and strain state, this is a stochastic process with an average rate of dislocations
75 forming and moving per (unit) volume. At higher strain rates, the finite dislocation velocity is not
76 sufficient to accommodate the fixed displacement rate, leading to a higher macroscopic yield stress.
77 Higher strain rates influence the microscopic behavior very similarly to lower temperatures: at a given
78 PEIERLS stress and a given stress state, fewer dislocations form or move. With increasing temperature,
79 activation energies increase, helping dislocations to move, which explains the observation of lower
80 strain rate sensitivities of flow stresses at 800 C compared to 25 C [69]. Between these temperature
81 levels, a maximum in strain rate sensitivity of flow stress is expected due to strain aging. Strain aging is
82 caused by COTTRELL atmospheres – carbon atoms pinned in dislocations, necessitating high (localized)
83 forces to unpin and thereby raising the (localized) force necessary to move the dislocation.

84   At high strain rates, adiabatic conditions promote locally high temperatures. These locally high
85 temperatures promote the strongly localized formation of shear bands: in the formation of dislocations,
86 only a portion of the expended energy is introduced into the crystal structure, another portion is
87 converted into heat [74], which leads to a locally higher temperature because at very high strain rates,
88 heat conduction is slow compared to heat generation. The higher temperature again facilitates the
89 generation of new dislocations, in which new heat is generated, leading to a cycle only broken by the
90 removal of the source of increasing strain. This may be a fracture event in monotonic loading or the
91 onset of unloading in cyclic loading. In the adiabatic regions, recrystallization may occur [75]. In cyclic
92 loading, strongly localized temperature increase depends on load level and pulse length. While the
93 global increase of temperature is well controlled by pulse pause methods, true localized temperatures
94 remain unknown to researchers. Localized temperatures in adiabatic conditions may be computed
95 based on a factor determining the share of energy converted into heat [69,76,77]. This factor has been
96 determined to be close to 100% [76].

97   At macroscopic scale, yield stress and ultimate tensile strength increase with increasing strain
98 rate [63,69,78,79]. A widespread model describing this relationship is the JOHNSON COOK model [80].

99   From a fracture mechanics point of view, fatigue is a crack growing from a pre-existing defect.
100 This defect may be e.g. an inclusion in the material, a scratch or in- and extrusions caused by persistent
101 slip bands. Crack growth rate is determined by an intrinsic crack growth curve and crack closure
102 effects [81]. Crack growth experiments on 32CrMo4 showed no overall influence of frequency (varied
103 between 0.02 Hz and 20 Hz, measured in the PARIS range) on the overall crack growth rate [82]. This
104 has been interpreted as absence of an influence of strain rate on the intrinsic crack growth curve [83].
105 To draw a generally applicable conclusion, more evidence is necessary, firstly regarding higher strain
106 rates and secondly regarding a wider range of carbon steels.

107   Plasticity-induced crack closure [81,84–89] depends on strain rate because plasticity depends on
108 strain rate. Kindly note that although the change in plasticity-induced crack closure is an intrinsic
109 effect with regard to intrinsic or extrinsic strain rate effects, the intrinsic crack growth curve is the one
110 measured without any plasticity-induced (or other) crack closure. For small polished specimens, the
111 influence of plasticity-induced crack closure is probably small since loads at the crack tip are below the
112 crack growth threshold until shortly before failure.

113   No fundamental difference has been observed between the strain rate dependencies of
114 deformations under cyclic compressive and cyclic tensile loads [64].

115 *2.2. Extrinsic Effects*

116   Specimens with larger critically loaded surface areas and volumes show decreased lifetimes
117 compared to specimens with smaller critically loaded surfaces and volumes. This phenomenon
118 is well-studied [90–103] and understood well enough to be included in design standards [104–106].

Ultrasonic fatigue specimens, i.e. all specimens used for very high strain rate fatigue tests, are generally small-sized. This introduces a bias if the size effect is not accounted for. JEDDI and PALIN-LUC [12] show that size effects explain the difference in results with different strain rates for several studies [42, 43,46] [3], which implies that there is no relevant strain rate effect in these studies. They [12] conclude that for high strength steels in general, there is no relevant strain rate effect on the fatigue behavior.

Another extrinsic effect is oxide-induced crack closure [81,84,86,88,107–110], which is caused by the following process: The outermost layer of the steel at the flanks of the crack is oxidized over time due to exposure to oxygen. Due to the oxidation, the volume of the outermost layer of the crack is increased. Due to the increased volume, the crack closes at higher loads. This leads to the crack being open for a lower portion of the load cycle which leads to the generation of fewer dislocations and therefore a lower amount of crack growth per cycle [111]. Although the usual thickness of oxide layers is only a few nanometer, at the crack flanks the oxide layer may grow to significant size due to continuous breaking and reforming due to fretting contact between both crack flanks [88]. Since at lower frequencies, more time passes between two cycles, the oxidation effect is stronger and the crack grows slower (less per cycle, not per time) than at higher frequencies. This implies a longer lifetime for low frequencies compared to high frequencies in the absence of other effects. This effect does not occur at high load ratios since the oxide layer is not sufficient to close the crack at high stresses.

Note that the oxide-induced crack closure effect does not dominate the influence of the atmosphere: the average lifetime of specimens tested in argon is longer than that of specimens tested in lab air all else being equal, Figures 9 and 10. A momentous difference has also been registered between dry air and humid air [112]. This effect has been reported to be pronounced in quenched 42CrMo4 steels [112]. The effect has been shown to decrease with tempering, ceasing to exist in 42CrMo4 tempered at 55 C for 1 h [112]. For a high hardness batch of 42CrMo4, no obvious difference has been observed in the fatigue life of specimens in high humidity air and specimens in high humidity argon, however it remains unclear if residual adsorbed oxygen in the specimens in argon may be responsible for the behavior [112]. For a 1076 MPa ultimate tensile strength batch of 41NiCrMo7-3-2 steel, slightly higher lifetimes were observed for specimens tested in dry air compared to specimens tested in humid air [113]. For 0.5% carbon steel, momentously longer lifetimes and a higher fatigue limit were observed in vacuum [114]. For 41NiCrMo7-3-2 [115] and 100Cr6 at a high load level [116], slightly longer lifetimes were observed in vacuum compared to lab air [115]. Specimens manufactured from 100Cr6 with artificial surface defects showed higher survival probabilities in lab air than in vacuum when tested at the same load level up to $2 \cdot 10^9$ cycles. Crack growth was observed to accelerate with increasing humidity in argon [117] and air [118,119]. In vacuum, reduced crack growth rates were observed in comparison to lab air [120,121].

The reduced fatigue performance in humid air and argon is largely blamed on the prevention of slip reversal – a mechanism that increases lifetime – in oxidizing environments in general [122–124]. Slip reversal occurs when dislocations are moved along a slip band onto the surface of the specimen during loading and are subsequentially moved back into their old position during unloading. This way, no damage accumulates and therefore, no contribution to failure is made. Adsorption of oxygen may prevent the reverse movement, which makes the slip irreversible [125]. Irreversible slip bands lead to intrusions and extrusions, which may nucleate a crack.

The oxide layers on the surface may have a higher YOUNGS modulus than the base steel. If that's the case, for dislocations to pass the interface, an additional force must be expended. This leads to pileups of dislocations just under the oxide layer, which promote crack initiation [124]. For aluminum – which shows a momentous influence of environment – however, it has been shown that the surface oxide has a lower YOUNGS modulus than the base metal [126,127].

---

[3] For this, a model assuming that fatigue strength is inversely proportional to specimen diameter is utilized. This model is meant to consider the effect of the critically loaded surface and volume, a consideration of the crack growth phase is not explicitly intended.

165 The environment of internal cracks may be viewed as a vacuum. This view is supported by
166 similar fracture surfaces [115,116,128]. The sometimes distinct segregation of cracks initiating from the
167 surface and cracks initiation from sub-surface with respect to the number of cycles to failure has been
168 attributed to the difference in crack initiation times in vacuum in comparison to lab air [129]. For a
169 batch of JIS-SNCM439, segregation was observed to be present if tests were conducted in lab air but
170 not if tests were conducted in vacuum [115].

171 In steels, hydrogen is present to some degree, although this degree is very low in high quality steel.
172 Some research [130,131] suggests that VHCF failure from inclusions is connected to hydrogen, even if
173 hydrogen concentrations are not measurable. This may be caused by an inhomogeneous distribution
174 of hydrogen in the specimen: hydrogen does not really follow FICK's law in its diffusion behavior but
175 concentrates at points of high tensile stress. At low strain rates hydrogen has a lot of time to diffuse to
176 the crack tip, at higher strain rates it has less time because the crack tip moves faster. The increased
177 hydrogen concentration implies shorter lifetimes for lower strain rates. In theory, all the hydrogen
178 in the whole specimen diffuses to an infinitesimal small volume around the crack tip because of the
179 stress singularity. The reality is of course less extreme. More on the interaction between hydrogen
180 diffusion and plasticity may be found in [132,133]. If hydrogen is introduced into or removed from the
181 specimen in any way during cyclic loading, this is generally a time dependent and therefore indirectly
182 strain rate dependent process. In specimens charged with hydrogen, crack growth rates increase
183 momentously with decreasing frequencies [83]. In uncharged austenitic specimens, crack growth rates
184 increase with decreasing frequencies, which has been attributed to non-diffusible hydrogen [83]. In
185 uncharged 34CrMo4 specimens, an increase of crack growth rate with decreasing frequency has not
186 been observed, which may be due to the much higher diffusivity of hydrogen [82,83]. These studies
187 were conducted at low strain rates. Due to the higher diffusivity, hydrogen diffusion may become more
188 influential in carbon steels at higher strain rates, however to our knowledge, there is no experimental
189 evidence available on this issue.

3. Experimental Foundation

191 In this work, the cyclic properties of the quenched and tempered steel 50CrMo4 are investigated.
192 The material was provided in five batches, having different tempering states with ultimate tensile
193 strengths σ_u of 919 MPa, 1096 MPa, 1170 MPa, 1475 MPa and 1726 MPa. Its chemical compositions are
194 given in Table 1 and tensile test results are given in Table 2.

195 Most data were obtained in two research projects on the influence of variable amplitude loading
196 in the VHCF range, conducted at the Centre for Engineering Materials (MPA-IfW) and Fraunhofer
197 LBF Darmstadt [5,6,10]. These are all data belonging to the material batches with tensile strengths of
198 919 MPa, 1170 MPa, 1475 MPa and 1726 MPa. The testing machines used therein for cyclic testing are
199 a 20 kHz ultrasonic testing system (USP), type BOKU Vienna UFTE, a 700 Hz electromechanic test
200 system (EMF) and a 400 Hz servo-hydraulic testing maschine (VHF), type Instron Schenck VHF 50D.
201 The results were obtained at testing frequencies of about 19 kHz for the USP, 700 Hz for the EMF and
202 20–200 Hz for the VHF.

203 For further validation, test data provided by Osnabrück University of Applied Sciences [8,134],
204 obtained at 20 kHz with an ultrasonic testing system (USPO) type BOKU Vienna and at about 95 Hz,
205 obtained with a electromechanic resonance testing machine, type Rumul Testronic (RTTO). The
206 investigated material was quenched and tempered to an ultimate tensile strength of 1096 MPa.

207 The ultrasonic testing equipment was operated in pulse pause mode. All tests were conducted
208 in ambient temperature. The load ratio was fixed to $R = -1$. At load ratios of -1, no cyclic creep
209 is observed in quenched and tempered carbon steel [142]. Therefore, cyclic creep is ignored in this
210 publication.

211 The fatigue specimen geometries are depicted in Figures 1 to 4. The metallographic
212 characterization of these specimens showed no irregularities relevant for this investigation, for more
213 details see [5,6,10,134].

Figure 1. Geometry of specimens with ultimate tensile strength 919 MPa and K=1 [9,10,40].

Figure 2. Geometry of specimens with ultimate tensile strength 1096 MPa and K=1.2 [8,134].

Figure 3. Geometry of USP specimens with ultimate tensile strength 919 MPa and K=1.75 [6], VHF specimens were finalized subsequently [9].

USP   VHF

Figure 4. Geometry of specimens with ultimate tensile strength 919 as well as 1726 MPa and K=2.06 [6].

Table 1. Chemical composition (in weight percent).

Material batch	C	Cr	Mo	Mn	P	S
919 MPa [5]	0.53	1.06	0.19	0.69	< 0.01	< 0.01
1096 MPa [8]	0.48	1.00	0.18	0.71	0.013	0.010
1170 MPa [10]	0.49	1.01	0.19	0.69	< 0.01	0.011
1475 MPa [10]	0.48	1.06	0.19	0.68	0.01	0.012
1726 MPa [6]	0.51	1.09	0.19	0.73	0.016	< 0.01

Table 2. Tensile test results.

Material batch	Young's modulus E in GPa	0.2% offset yield strength $\sigma_{0.2}$ in MPa	ultimate tensile strength σ_{u} in MPa
919 MPa [5]	206	842	919
1096 MPa [8]	202	1000	1096
1170 MPa [10]	208	1025	1170
1475 MPa [10]	204	1345	1475
1726 MPa [6]	215	1544	1726

To asses the material behavior at high strain rates, fast tensile tests were conducted on a high speed tensile testing machine. On the left hand side of Figure 5, the ultimate tensile strength results for the 919 MPa batch as well as a bi-linear approximation thereof are shown. On the right hand side, these data are combined with data from the 1170 MPa batch and from the 1475 MPa batch. For comparison, the stress is normalized to the particular quasi-static ultimate tensile strength, see Table 2. All three materials show a good agreement in their relative 0.2% offset yield strength $\sigma_{0.2}$. In the tests on the 1170 MPa batch at strain rates of about 15/s, two outliers were observed. In a comparative metallographic examination of an outlier specimen and a non-outlying specimen, the outlier showed a significantly different microstructure. In this investigation, the outliers are considered in the process of fitting the bi-linear curve to uphold consistency since not all specimens were investigated with regard to their microstructure. The fatigue behaviors of the batches 1170 MPa and 1475 MPa are not assessed in this study because the inhomogenities in the microstructure state were also observed in some cyclic test specimens and therefore, the comparability of the fatigue behavior is limited.
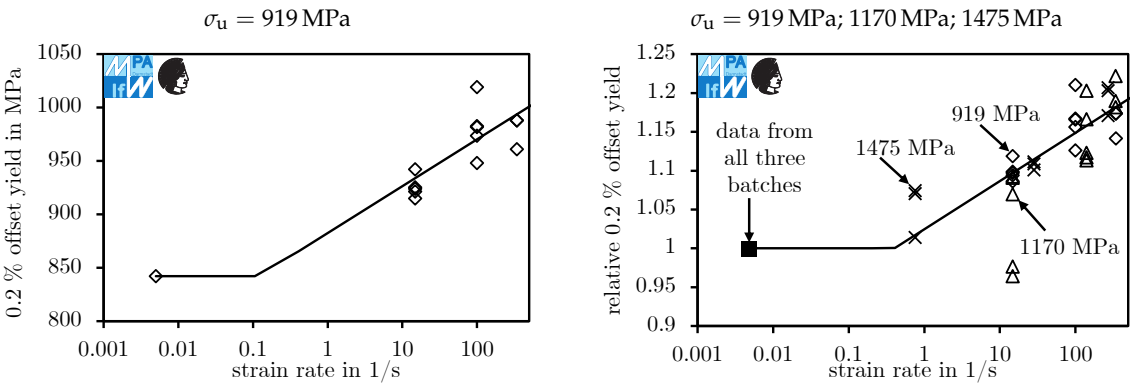
Figure 5. 0.2% offset yield depending on the strain rate, for the 919 MPa ultimate tensile strength (left) and for the batches 919 MPa, 1170 MPa and 1475 MPa (right).

In Figure 6, the stabilized cyclic stress strain test results are shown. The left diagrams show test results for the 919 MPa and 1726 MPa batch. These results were obtained in five constant amplitude

tests each. On the right hand side, the results for the 1096 MPa batch are given in the first row. These
were obtained in an Incremental Step Test. As shown in the bottom right diagram, the test results fit
together well, since the stress amplitude over strain amplitude values increase with the quasi static
ultimate tensile strength of the material, regardless of the test setting.
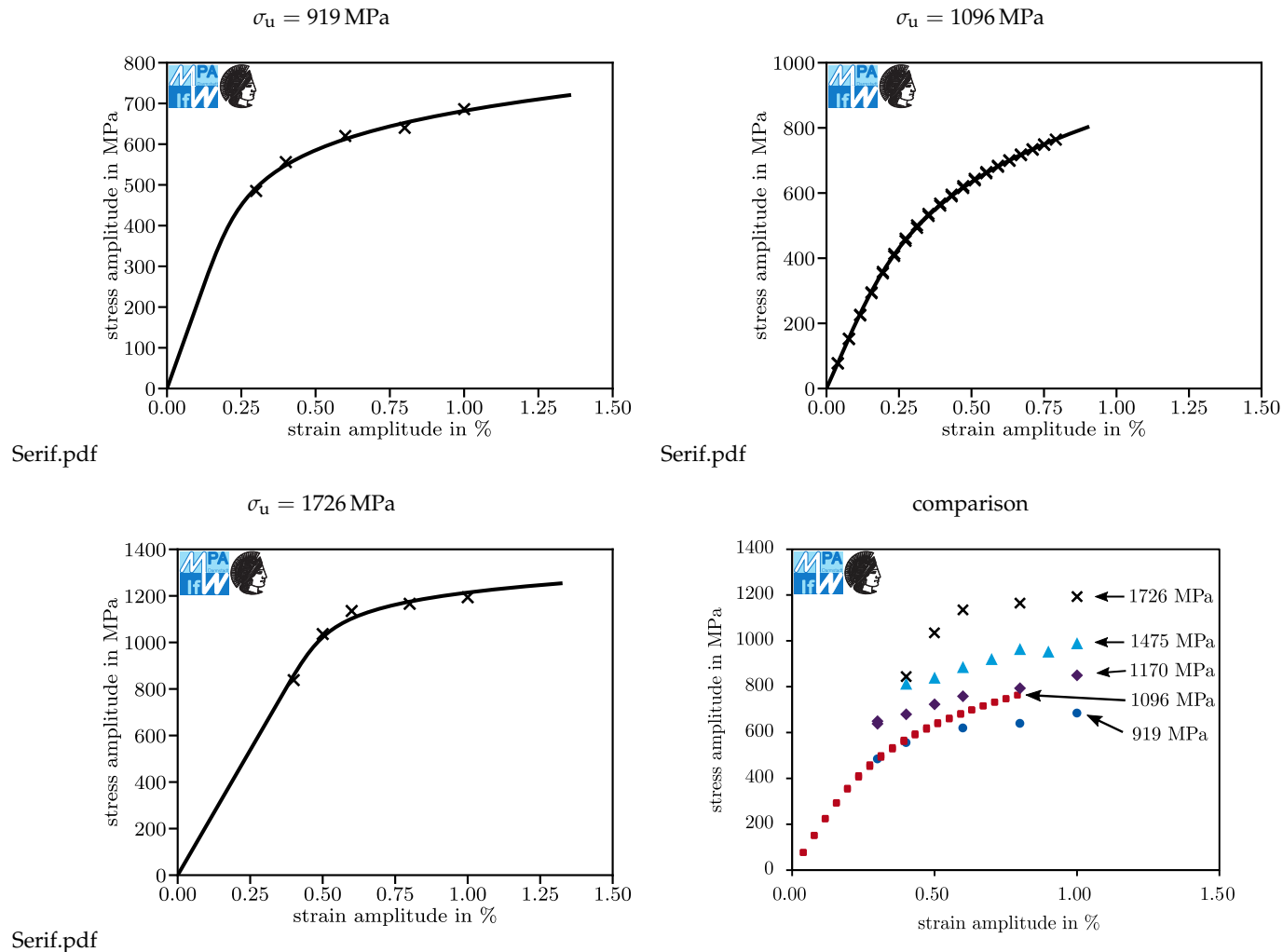
Figure 6. Cyclic stress strain curves. First row: 919 MPa and 1096 MPa ultimate tensile strength. Second
row: 1726 MPa ultimate tensile strength (left) and comparison of batches with 919 MPa, 1096 MPa,
1170 MPa, 1475 MPa and 1726 MPa ultimate tensile strength.

The cyclic stress strain curve was generated in a least squares fit in stress direction using the
RAMBERG–OSGOOD formulation [135],

$$\varepsilon_a = \epsilon_{a,el} + \epsilon_{a,pl} = \frac{\sigma_a}{E} + \left(\frac{\sigma_a}{K'}\right)^{1/n'}, \tag{1}$$

where ε_a is the strain amplitude, σ_a is the stress amplitude, K' is the cyclic hardening coefficient and n'
is the cyclic hardening exponent. The parameters obtained for the cyclic stress strain curves provided
in the previous figures are summarized in Table 3.

Table 3. Cyclic material constants.

Material batch	Young's modulus E in GPa	hardening coefficient K' in MPa	hardening exponent n'
919 MPa	206	1341	0.135
1096 MPa	202	2816	0.237
1170 MPa	204	1162	0.068
1475 MPa	204	1436	0.073
1726 MPa	215	1687	0.060

4. Method

4.1. Correction for Control Type

The stress levels of displacement controlled tests are corrected using the NEUBER rule [136,137]. Therein, cyclic stress strain curves are used. These curves were obtained either from constant amplitude tests or from Incremental Step Tests by fitting a RAMBERG–OSGOOD curve [135], Figure 6. These RAMBERG–OSGOOD curves are corrected for the specific strain rate, assuming that the cyclic offset yield strength increases proportionally to the monotonous offset yield strength with increasing strain rate. The monotonous offset yield strength was modeled by a bi-linear function in log-lin space, Figure 5. A constant strain rate is assumed, while the strain rate in fact is sinusoidal; the computed strain rate is equal to the real average strain rate.

The strain amplitude ϵ_a according to RAMBERG–OSGOOD is computed as the sum of the elastic strain amplitude $\epsilon_{a,el}$ and the plastic strain amplitude $\epsilon_{a,pl}$, which may be computed from the stress amplitude σ_a, the 0.2% offset yield strength $\sigma_{0.2}$, the yield offset α, Young's modulus E and the RAMBERG–OSGOOD exponent n:

$$\epsilon_a = \epsilon_{a,el} + \epsilon_{a,pl} = \frac{\sigma_a}{E} + \alpha \frac{\sigma_a}{E} \left(\frac{\sigma_a}{\sigma_{0.2}} \right)^{n-1} \tag{2}$$

This formulation differs from the formulation in Eq. 1 only in the variables used, the relationships between the variables are $n = \frac{1}{n'}$ and $\alpha = \left(\frac{E}{K'} \right)^n \left(\frac{\sigma_{0.2}}{E} \right)^{n-1}$. Here, the less customary version of the formula is used because the offset yield strength $\sigma_{0.2}$ is explicit, which is advantageous for the algorithm. The yield offset α is computed as:

$$\alpha = \frac{0.002 \, E}{\sigma_{0.2}} \tag{3}$$

The cyclic offset yield strength $\sigma_{0.2}$ is strain rate dependent and therefore computed based on the ratio of the strain rate $\dot{\epsilon}$ and the reference strain rate $\dot{\epsilon}_{ref}$. To model the behavior, the bi-linear function x is used:

$$\sigma_{0.2}(\dot{\epsilon}) = \sigma_{0.2}(\dot{\epsilon}_{ref}) \cdot x \left(\frac{\dot{\epsilon}}{\dot{\epsilon}_{ref}} \right) \tag{4}$$

The strain rate $\dot{\epsilon}$ is computed using the strain amplitude ϵ_a and the frequency f, assuming that the strain rate was constant during a single fatigue test:

$$\dot{\epsilon} = 4 \cdot \epsilon_a \cdot f \tag{5}$$

NEUBER's rule is applied by finding the point in the RAMBERG–OSGOOD formulation of the cyclic material behavior (Eq. 2) for which the strain energy density is equal to the strain energy density in the elastic computation, which is derived from the elastically computed stress amplitude and the elastically computed strain amplitude :

$$\min_{\sigma_a}(\sigma_a \cdot \epsilon_a(\sigma_a) - \sigma_{a,\text{elastic}} \cdot \epsilon_{a,\text{elastic}})^2 \tag{6}$$

Since the RAMBERG–OSGOOD formulation is not static but depends on the strain rate, the optimization problem is solved iteratively and in each iteration, the strain rate from the last iteration is used. The solving of the minimization problem is repeated until the change in $\dot{\epsilon}$ over an iteration comes below a threshold. For this investigation, the threshold 10^{-15} was used. The computation procedure is displayed in Figure 7. Due to the iterative character of the algorithm, an index i is added to some variables.
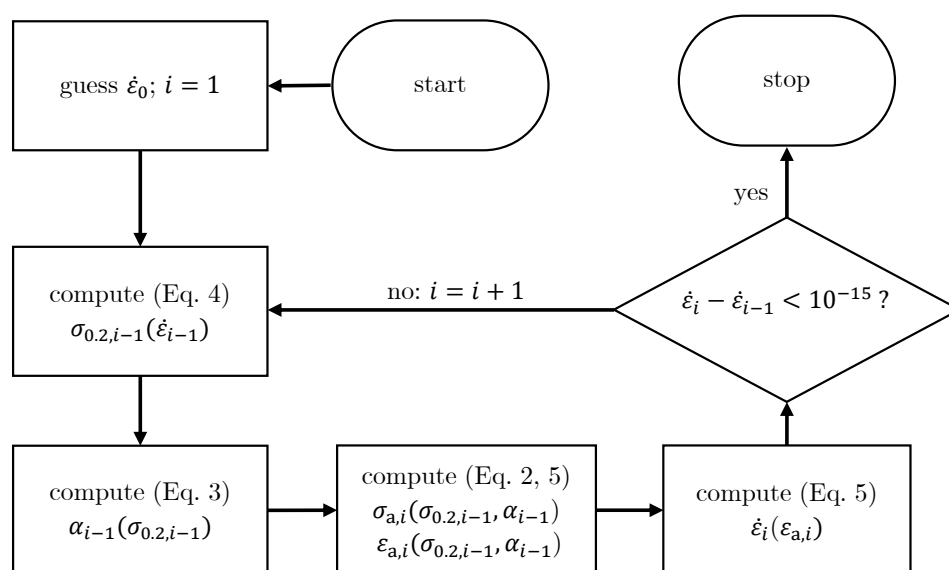
Figure 7. Algorithm used in this study to compute corrected load levels.

An earlier version of the algorithm used herein is described in [40]. The difference between both versions of the algorithm is that the algorithm used herein models the offset yield strength as a bi-linear function while the algorithm described there utilizes a linear function. The change made for this study leads to slightly smaller correction offsets at high strain rates and slightly higher offsets at low strain rates (as long as these low strain rates are above the lowest strain rate tested). The change is motivated by the fact that for medium to low strain rates, the offset yield strength is not a function of the strain rate.

4.2. Statistical Analysis

The goal of the correction is to create data from displacement controlled cyclic tests that agree well with data from force controlled cyclic tests. To evaluate whether the agreement is improved by the correction, a statistical analysis is conducted. Two types of data sets are created, merging results of displacement controlled cyclic tests before (type 1) and after (type 2) correction with results of force controlled cyclic tests.

For each data set, a lifetime model assuming a linear course of the fatigue curve in log-log space and a constant log-normal distribution of fracture cycles at given load levels is fitted to all events occurring at up to $3 \cdot 10^6$ cycles, using the Maximum Likelihood Method. For these models, the logarithmic standard deviation is estimated in the fitting process.

The log-normal distribution is generally accepted as a good approximation of the fatigue behavior of steels in the HCF range [138–141]. Overall, the assumption of log-normality is reasonable although some of the data sets under investigation deviate significantly from log-normal distributions: in data

sets with two populations that differ from each other in their average lifetimes at a given load level (e.g. due to different control types), the assumption of a log-normal distribution is obviously not true. More data on the question whether the data sets under investigations are well described by models using constant log-normal distributions may be found in the appendix.

The estimated standard deviation provides an intuitive measure of the agreement between two underlying data sets: if the points of both data sets are far away from each other, the estimated standard is high and the intuitively estimated agreement is low. If the points of each data set are close to the point of the other data set, the estimated standard deviation is low and the intuitively estimated agreement is high.

To further reduce subjectivity, the agreement is also evaluated using the mathematically motivated measure of the log-likelihood function. A higher log-likelihood value implies a better agreement of all data in the data set and therefore also implies a better agreement between both merged data sets. Therefore, the log-likelihood value is used as an objective comparative measure of agreement.

5. Results

All tests performed with electromagnetic and servo-hydraulic testing machines were conducted force controlled, whereas the ultrasonic testing system operates displacement controlled. In Figure 8, the fatigue behavior, namely the stress amplitudes plotted against the number of cycles for specimens quenched and tempered to ultimate tensile strength levels of 919 MPa are given. The tests were conducted with unnotched round specimens (stress concentration factor $K_t = 1$) in laboratory air. On the left hand side, a purely elastic material law was used for evaluation. The data presented there has not undergone any correction. On the right hand side, the displacement controlled test results were corrected using the elastic-plastic material law given in section 3 and the method described in section 4.1. The continuous lines depict the fatigue curves for 50% survival probability, the dashed ones for 10% and 90%, respectively. The curves were generated using the Maximum Likelihood Method, fitting the slope exponent k_1, the standard deviation SD and a reference point of the fatigue curve [4] . For the generation of these curves, only events occurring at up to $3 \cdot 10^6$ cycles were taken into account.

---

[4] The fatigue curve describes a field of failure probability densities f with the reference logarithmic number of cycles $N_{\text{ref,log}}$, the reference logarithmic normalized stress amplitude $\sigma_{\text{ref,log}}$ and the logarithmic standard deviation SD that depends on the logarithm of the number of cycles N_{log} and the logarithm of the normalized stress amplitude $\sigma_{\text{amplitude,log}}$:

$$f(N_{\text{log}}, \sigma_{\text{amplitude,log}}) = \frac{1}{\sqrt{2\pi SD^2}} \exp\left(-\frac{\left(N_{\text{log}} - N_{\text{ref,log}} - \left(\sigma_{\text{amplitude,log}} - \sigma_{\text{ref,log}}\right) \cdot k_1\right)^2}{2\,SD^2}\right)$$
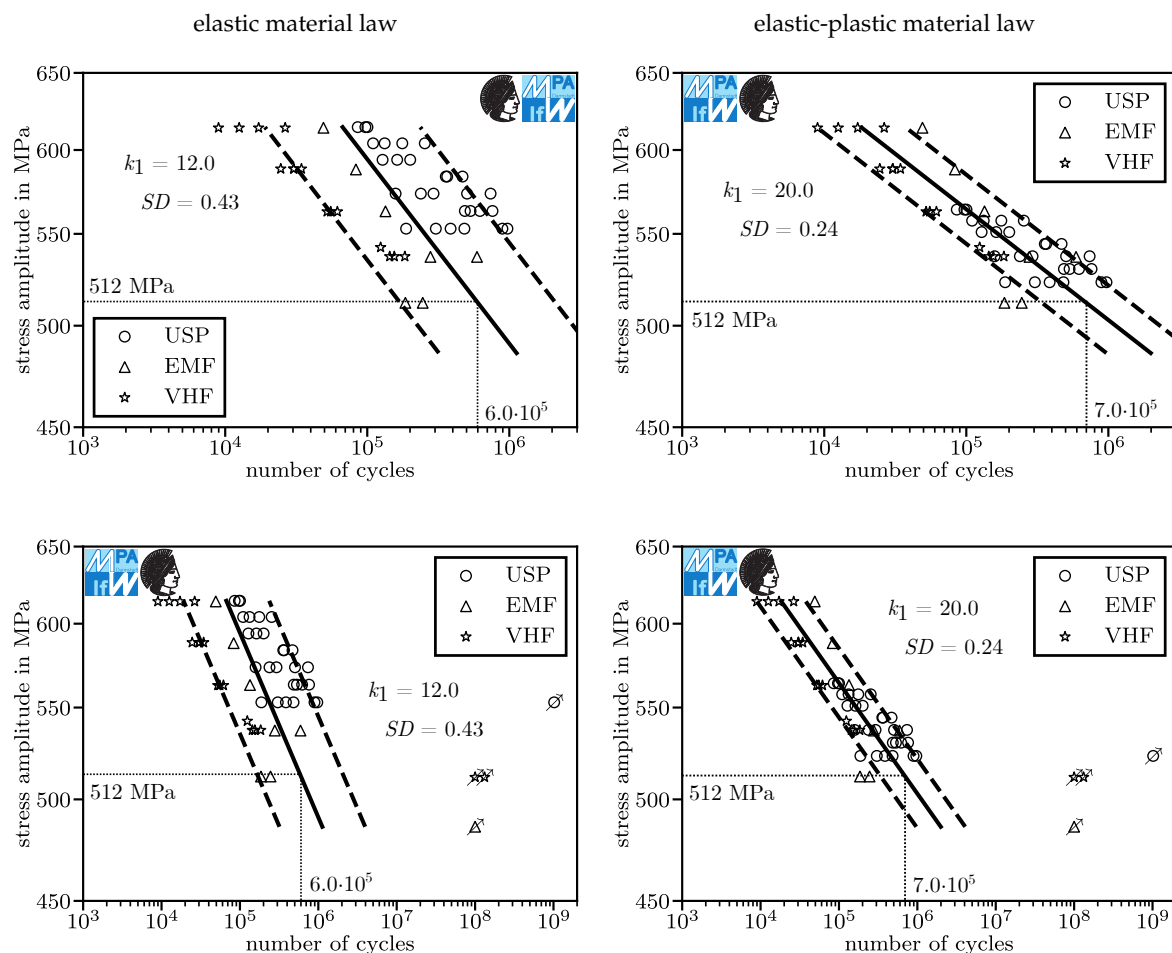
Figure 8. Fatigue behavior of 50CrMo4 in laboratory air; 919 MPa ultimate tensile strength; $K_t = 1$; Curves of 10, 50 and 90% probability of survival; run-outs are marked with an arrow; left side: before correction; right side: after correction; top: only HCF region; bottom: including VHCF region.

In the HCF range (top row of Figure 8), specimens tested with the USP machine last longer at a certain load level compared to the force controlled machines EMF and VHF, if the stress was calculated using the linear elastic material law (left column). After applying the correction by using the elastic-plastic material law (right column), the USP data points were all moved to a lower load level and agree better with the other results. The EMF and VHF results were not changed. Thereby, the slope exponent increases from $k_1 = 12.0$ to $k_1 = 20.0$ after correction and the standard deviation of the fatigue curve reduces from 0.43 to 0.24. In the bottom row diagram, the VHCF region may be observed. The run-out obtained on the USP is moved closer to the run-outs of the EMF and the of VHF. In the corrected data, the results of the VHF occur earlier than results obtained on the other testing setups, except the lowest load level of the EMF.

To objectively evaluate whether the improvement of the fit is significant, a t-test is conducted against the null-hypothesis that the average logarithmic deviation of the fracture events from the 50% lifetime prediction is the same for both the evaluation with correction and the evaluation without correction. The logarithmic deviation is measured horizontally. Since both curves are obtained using the same specimens, a paired-sample test is conducted. With predicted logarithmic lifetimes according to the model with correction $N_{\log,\text{predicted,corr},i}$ and according to the model without correction $N_{\log,\text{predicted,no\_corr},i}$ as well as the measured lifetimes $N_{\log,\text{fracture},i}$, differences in logarithmic prediction error $\Delta N_{\log,i}$ are computed and used to compute the t-statistic and the p-value according to statistical standard theory utilizing the Python module SciPy [143].

$$\Delta N_{\log,i} = |N_{\log,\text{fracture},i} - N_{\log,\text{predicted,corr},i}| - |N_{\log,\text{fracture},i} - N_{\log,\text{predicted,no\_corr},i}| \tag{7}$$

The null hypothesis H_0 and the hypothesis H_1 are mathematically defined as:

$$H_0 : \sum_i \Delta N_{\log,i} = 0 \quad \text{vs.} \quad H_1 : \sum_i \Delta N_{\log,i} \neq 0 \tag{8}$$

Computation yields a t-statistic of 6.3 at 49 degrees of freedom and a p-value $7.5 \cdot 10^{-6}$%.[5] At a 5% threshold for significance, the difference in prediction quality is statistically significant and the null hypothesis is rejected. Kindly note that this only applies to the batch under investigation, not for 50CrMo4 in general. The average magnitudes of the logarithmic prediction error are 0.376 without and 0.203 with correction.

The observations made about the results presented in Figure 8 also hold true for test results of notched specimens with $K_t = 1.75$ that were quenched and tempered to ultimate tensile strength levels of 919 MPa, tested in laboratory air, see Figure 9. If the stress was calculated using the elastic material law, the USP specimens also last longer at a given stress level. The correction routine decreases the standard deviation from 0.20 to 0.16. The run-outs are moved further apart. Before correction, the fracture events obtained on the VHF occur earlier (tend to be on the left side of the fatigue curve for 50% survival probability) than fracture events obtained on the USP (which tend to be on the right side of the fatigue curve for 50% survival probability). After correction, this relationship is inverted.

Testing the difference in logarithmic prediction error $\Delta N_{\log,i}$ according to Equation (7) yields a t-statistic of 1.1 at 15 degrees of freedom and a p-value of 28.8%, which implies that the null hypothesis cannot be rejected based on the data available. Absence of evidence is not evidence of absence. The low p-value may be caused by unfavorable randomness or low number of specimens. Additional tests may yield significant results. The average magnitudes of the logarithmic prediction error are 0.174 without and 0.137 with correction.

elastic material law   elastic-plastic material law

Figure 9. Fatigue behavior of 50CrMo4 in laboratory air; 919 MPa ultimate tensile strength; $K_t = 1.75$; Curves of 10, 50 and 90% probability of survival; run-outs are marked with an arrow; left side: before correction; right side: after correction; top: only HCF region; bottom: including VHCF region.

Figure 10 shows the results for notched specimens with $K_t = 1.75$ quenched and tempered to ultimate tensile strength levels of 919 MPa, tested in an argon inert gas atmosphere. The diagrams before and after correction show a very similar behavior compared to the previous tests. This data set includes an outlier failure on the VHF. This outlier cannot be explained by the correction method. Kindly note the extremely low standard deviation of 0.11 after correction (ignoring the outlier since it occurred at over $3 \cdot 10^6$ cycles). While we would expect tests in argon to yield results with lower scatter due to a controlled atmosphere, the reduced standard deviation may also be caused by the elimination of extrinsic effects, e.g. oxide-induced crack closure.

In fact, if there was a momentous bias between the data obtained on the USP compared to the data obtained on the VHF, the standard deviation would be greater. Therefore, the bias must be small. Consequently, the sum of all intrinsic and extrinsic effects not accounted for is small. The natural

---

[5] Simplified, a p-value of $7.5 \cdot 10^{-6}$% means: If the true average of $\Delta N_{\log,i}$ was zero, there would be a $7.5 \cdot 10^{-6}$% chance to obtain a mean with a magnitude as great or greater than we actually obtained. Less simplified, this includes the assumption that our estimated standard deviation is true. Overly simplified, we are $100\% - 7.5 \cdot 10^{-6}\% = 99.99...\%$ certain that the correction for control type leads to models with lower prediction error, which is, strictly speaking, wrong.

conclusion is that the individual effects are small, however more research is necessary to eliminate the possibility that the effects are large and cancel each other out.

Some atmospheric influences, e.g. oxide-induced crack closure, lead to a longer lifetime for low frequencies compared to high frequencies, see section 2.2. Longer lifetimes at low frequencies can be observed in Figure 9 (laboratory air, 6 out of 7 USP results on the left side of the 50% fatigue curve) but not in Figure 10 (argon, 4 out of 7 USP results on the left side of the 50% fatigue curve) on the right. The underlying experiments only differ in the atmosphere and the load levels, the specimens were from the same batch. At the current state of research, the atmospheric influences are the best explanation for the difference in lifetime since intrinsic effects can be ruled out since they would also occur in argon.

The average lifetime of specimens tested in argon is longer than that of specimens tested in lab air all else being equal, Figures 9 and 10. At first, this seems to be in dissent with the observation of different lifetime prolongations due to atmospheric influences. This ostensible contradiction can be explained by the dominance of the effect of the prevention of slip-reversal, which only requires small amounts of oxygen in the atmosphere and does not depend on frequency in lab air because the oxygen concentration there exceeds the necessary concentration by orders of magnitude (for more on this effect, see section 2.2).

Testing the difference in logarithmic prediction error $\Delta N_{\log,i}$ yields a t-statistic of 2.3 at 15 degrees of freedom and a p-value of 3.5%, which implies significance. The average magnitudes of the logarithmic prediction error are 0.288 without and 0.174 with correction.

elastic material law   elastic-plastic material law

Figure 10. Fatigue behavior of 50CrMo4 in argon; 919 MPa ultimate tensile strength; $K_t = 1.75$; Curves of 10, 50 and 90% probability of survival; run-outs are marked with an arrow; left side: before correction; right side: after correction; top: only HCF region; bottom: including VHCF region.

Regarding the test results for notched specimens with a stress concentration factor of $K_t = 2.06$, the data obtained in the HCF range show a better agreement, see first row of Figure 11. The fracture events in the VHCF range (second row) also show a higher concordance after correction, but are obviously not comprised within the linear fatigue curve approximation. Hence, a bi-linear approximation of the fatigue curve is necessary to comply with the data, which is out of scope for this paper.

Testing the difference in logarithmic prediction error $\Delta N_{\log,i}$ yields a t-statistic of 2.6 at 40 degrees of freedom and a p-value of 1.3%, which implies significance. The average magnitudes of the logarithmic prediction error are 0.719 without and 0.640 with correction.

elastic material law   elastic-plastic material law

Figure 11. Fatigue behavior of 50CrMo4 in laboratory air; 919 MPa ultimate tensile strength; $K_t = 2.06$; run-outs are marked with an arrow; left side: before correction; right side: after correction; top: only HCF region; bottom: including VHCF region.

The results for specimens with a slight stress concentration of $K_t = 1.2$, quenched and tempered to ultimate tensile strength levels of 1096 MPa, tested in laboratory air are given in Figure 12. In the HCF range, the non-corrected data show a higher lifetime at similar stress levels (around 625 MPa stress amplitude) for tests conducted with the ultrasonic testing machine USPO compared to those obtained with an electromagnetic resonance testing machine (RTTO). After correction, the stress amplitudes match better and the standard deviation reduces – even though there is still a distinct scatter range. Regarding the VHCF range (second row), the stress level of the USPO run-outs is reduced, even though it is still quite high, compared to the results obtained with the RTTO. The observed differences in fatigue behavior are partially or completely caused by differences in specimen geometry. Since the

interaction between correction for control type and correction for critically loaded surface area is a nontrivial problem that requires an evaluation of its own, we do not conduct the correction for critically loaded surface area here.

Testing the difference in logarithmic prediction error $\Delta N_{\log,i}$ yields a t-statistic of 1.6 at 29 degrees of freedom and a p-value of 12.2%, which implies rejection of significance. The average magnitudes of the logarithmic prediction error are 0.295 without and 0.276 with correction.

elastic material law   elastic-plastic material law

Figure 12. Fatigue behavior of 50CrMo4 in laboratory air; 1096 MPa ultimate tensile strength; $K_t = 1.2$; run-outs are marked with an arrow; left side: before correction; right side: after correction; top: only HCF region; bottom: including VHCF region.

Figure 13 depicts the test results for specimens quenched and tempered to ultimate tensile strength levels of 1726 MPa. Notched specimens with $K_t = 2.06$ were tested in laboratory air. Here, the proposed correction does not show a relevant change because of the comparably high cyclic 0.2% offset yield strength stress and especially high strain rates.

Testing the difference in logarithmic prediction error $\Delta N_{\log,i}$ yields a t-statistic of 1.04 at 31 degrees of freedom and a p-value of 30.5%, which implies rejection of significance. The very high p-value is not surprising because the intersubjective impression is that there is no relevant difference between both data sets. The average magnitudes of the logarithmic prediction error are 0.159 without and 0.162 with correction, meaning that the method for correction worsened prediction quality (insignificantly).

To determine whether there is an overall positive influence on the logarithmic prediction error $\Delta N_{\log,i}$, a t-test according to (8) is conducted using data from all cyclic tests presented above. The test yields a t-statistic of 6.5 at 184 degrees of freedom and a p-value of $7.1 \cdot 10^{-8}\%$.

elastic material law   elastic-plastic material law

Figure 13. Fatigue behavior of 50CrMo4 in laboratory air; 1726 MPa ultimate tensile strength; $K_t = 2.06$; run-outs are marked with an arrow; left side: before correction; right side: after correction; top: only HCF region; bottom: including VHCF region.

In Table 4, the parameters of the fatigue curves in Figures 8 to 13 are summarized. Regarding the slope exponent k_1, there is no trend whether the slope increases or decreases after correction. In all tests conducted, the standard deviation SD decreases or remains unchanged after correction. Furthermore, for all test results, the logarithmic likelihood value $L_{\log}$ increases, which implies that the corrected regression lines fit the test results better than the non-corrected ones.

Table 4. Parameters, log-likelihood values of fitted fatigue curves as well as number of specimens and p-values obtained in t-test.

	σ_u	K_t	atmosphere	corrected?	σ_ref	N_ref	k_1	SD	L_log	# specimens p-value
Figure 8	919 MPa	1	lab air	no	512 MPa	$6.0\cdot10^5$	12.0	0.43	-28.4	50
Figure 8	919 MPa	1	lab air	yes	512 MPa	$7.0\cdot10^5$	20.0	0.24	-0.4	$7.5\cdot10^{-6}$%
Figure 9	919 MPa	1.75	lab air	no	630 MPa	$3.3\cdot10^5$	11.9	0.20	3.2	16
Figure 9	919 MPa	1.75	lab air	yes	574 MPa	$3.4\cdot10^5$	8.5	0.16	6.5	28.8%
Figure 10	919 MPa	1.75	argon	no	630 MPa	$1.1\cdot10^6$	13.7	0.27	-1.5	16
Figure 10	919 MPa	1.75	argon	yes	574 MPa	$1.1\cdot10^6$	10.3	0.11	11.2	3.5%
Figure 11	919 MPa	2.06	lab air	no	618 MPa	$3.8\cdot10^5$	5.8	0.39	-16.1	41
Figure 11	919 MPa	2.06	lab air	yes	566 MPa	$4.7\cdot10^5$	6.3	0.30	-7.2	1.3%
Figure 12	1096 MPa	1.2	lab air	no	500 MPa	$3.6\cdot10^5$	2.3	0.37	-12.34	30
Figure 12	1096 MPa	1.2	lab air	yes	500 MPa	$5.1\cdot10^5$	5.2	0.34	-10.2	12.2%
Figure 13	1726 MPa	2.06	lab air	no	876 MPa	$4.8\cdot10^5$	9.2	0.22	3.6	32
Figure 13	1726 MPa	2.06	lab air	yes	875 MPa	$4.8\cdot10^5$	9.4	0.22	3.6	30.6%

Complementing the intuitive interpretation of Table 4, statistical tests were conducted. A paired-sample t-test was conducted for the log-likelihoods. The differences in log-likelihood, 28.0, 3.3, 12.7, 8.9, 2.14 and 0.0, yield a t-statistic of 2.17, which translates to a p-value of 8.2%.[6] The average difference of the log-likelihoods is 9.2. At a 5% threshold for acceptance of significance, the reduction of log-likelihood is not significant. As per usual in science and especially in statistical testing, absence of evidence is not evidence for absence. In the case of the log-likelihood, this means that the reason for not rejecting the null hypothesis may well be the low sample number of 6 and the high standard deviation which was estimated to be 10.3.

Another paired-sample t-test was conducted for the standard deviations. The differences in standard deviation, 0.19, 0.04, 0.16, 0.09, 0.03 and 0.00, yield a t-statistic of 2.74, which translates to a p-value of 4.1%. Therefore, the reduction of standard deviation is significant considering the threshold of 5%. The average difference in standard deviation is 0.085. This implies that the method for correction for control type significantly decreases standard deviation not only of the data sets under investigation but also of all data sets generated in similar tests on batches of 50CrMo4 that are comparable to the ones under investigation.

Testing the average magnitudes of logarithmic prediction error of the six different tests in a paired-sample t-test yields a t-statistic of 2.68 which translates to a p-value of 4.4% at average magnitudes of logarithmic prediction errors of 0.335 without and 0.265 with correction for control type. This also implies significance.

6. Conclusion

In this study, cyclic test results obtained in displacement controlled cyclic tests at about 20 kHz were corrected for control type. Two kinds of combined sets were created. The first kind of set contains cyclic test results from force controlled tests and uncorrected results from displacement controlled tests. The second kind of set contains cyclic test results from force controlled tests and control type corrected results from displacement controlled tests.

---

[6] Simplified, a p-value of 8.2% means: If the true average difference between log-likelihood values obtained with and without correction was zero, there would be a 8.2% chance to obtain a mean with a magnitude as great or greater than we actually obtained in six draws. Less simplified, this includes the assumption that the true standard deviation of the difference of log-likelihoods is exactly the one we estimated. Overly simplified, we are $100\% - 8.2\% = 91.8\%$ sure that the correction for control type leads to models with higher log-likelihood values, which is, strictly speaking, wrong.

⁴⁴⁹ The agreement of the cyclic test results with each other inside each data set created this way was
⁴⁵⁰ quantified through the standard deviation and the likelihood value of a model fitting the data set
⁴⁵¹ in the HCF range. Throughout the investigation, the agreements of the data sets with control type
⁴⁵² corrected data from displacement controlled tests were equal or superior to the agreements of the
⁴⁵³ data sets with uncorrected data from displacement controlled tests. This means that the correction
⁴⁵⁴ method offers significantly improved comparability of displacement controlled cyclic tests with force
⁴⁵⁵ controlled cyclic tests in the HCF range. In the VHCF range, additional investigations are necessary.

⁴⁵⁶ For 50CrMo4, the state of research regarding the influence of the strain rate on the fatigue life
⁴⁵⁷ may be advanced by incorporating the method presented in this paper. A higher strain rate effect has
⁴⁵⁸ been reported in low strength 50CrMo4 than in high strength 50CrMo4. However, the difference in
⁴⁵⁹ strain rate effects may have been overestimated due to an accidental bias in experimental design: the
⁴⁶⁰ state of research is based on experiments in which low strength 50CrMo4 was tested at load levels
⁴⁶¹ momentously exceeding its cyclic yield strength but high strength 50CrMo4 was tested only at load
⁴⁶² levels under or just over its cyclic yield strength. In these experiments, strain rate effects cannot be
⁴⁶³ separated from control type effects statistically. An analysis of the experimental data considering and
⁴⁶⁴ correcting for control type effects would reduce and may practically eliminate the observed difference
⁴⁶⁵ in strain rate effects[7]. Especially the extremely low standard deviation for the specimens tested in
⁴⁶⁶ argon implies only a small intrinsic strain rate effect for low strength 50CrMo4.

⁴⁶⁷ Appendix: Do models assuming log-normal distributions describe the data sets well?

⁴⁶⁸ In this appendix, we investigate whether models assuming normal distributions describe the
⁴⁶⁹ data sets under investigation well. To this means, all fatigue events with numbers of cycles to failure
⁴⁷⁰ up to $3 \cdot 10^6$ of each test set are shifted to a single virtual load level and compared graphically to the
⁴⁷¹ cumulative probability function of the fitted log-normal distribution. The relative numbers of cycles
⁴⁷² until failure are standardized over the estimated standard deviations, Figures 14 to 19.
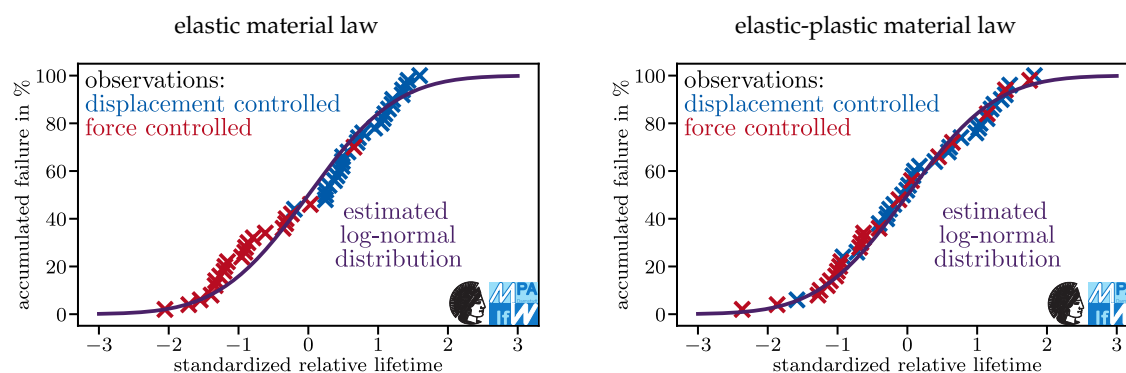
Figure 14. Estimated and observed accumulated failure rates for 50CrMo4 specimens in laboratory air;
919 MPa ultimate tensile strength; $K_t = 1$.

---

[7] The current state of research is consistent with theoretical considerations: in low strength 50CrMo4, the strain rate dependent
PEIERLS stress makes up a greater share of the total load stress necessary to move a dislocation than in high strength
50CrMo4. Stresses caused by nearby dislocations do not depend on strain rate. However, this does not include any
prediction of the size of the strain rate effect, therefore a strain rate effect close to zero in low strength 50CrMo4 would also
be consistent with theoretical considerations
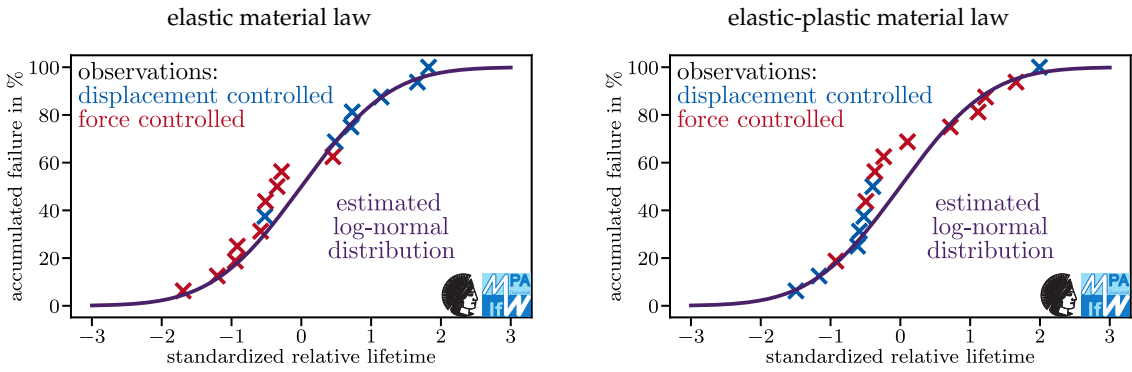
Figure 15. Estimated and observed accumulated failure rates for 50CrMo4 specimens in laboratory air; 919 MPa ultimate tensile strength; $K_t = 1.75$.
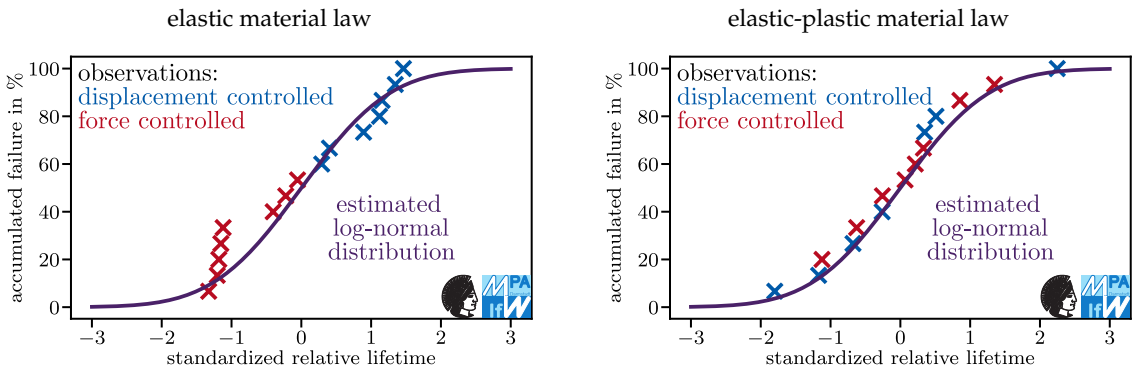
Figure 16. Estimated and observed accumulated failure rates for 50CrMo4 specimens in argon; 919 MPa ultimate tensile strength; $K_t = 1.75$.
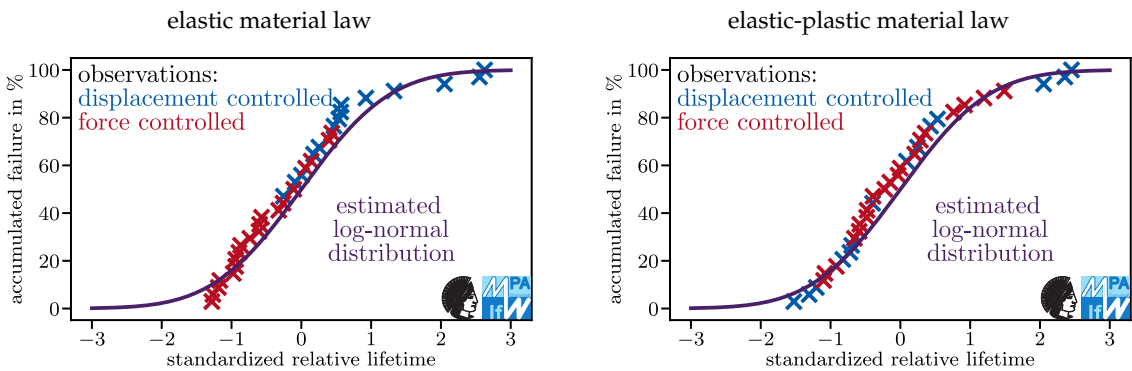
Figure 17. Estimated and observed accumulated failure rates for 50CrMo4 specimens in laboratory air; 919 MPa ultimate tensile strength; $K_t = 2.06$.
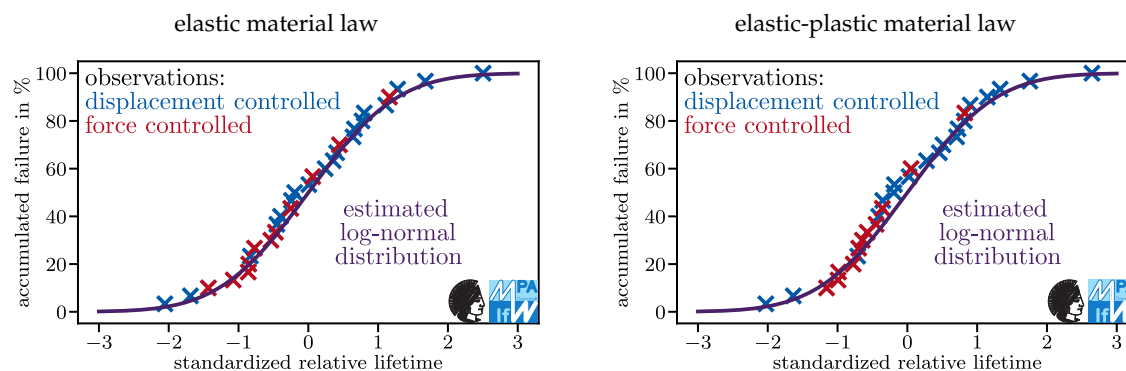
Figure 18. Estimated and observed accumulated failure rates for 50CrMo4 specimens in laboratory air; 1096 MPa ultimate tensile strength; $K_t = 1.2$.
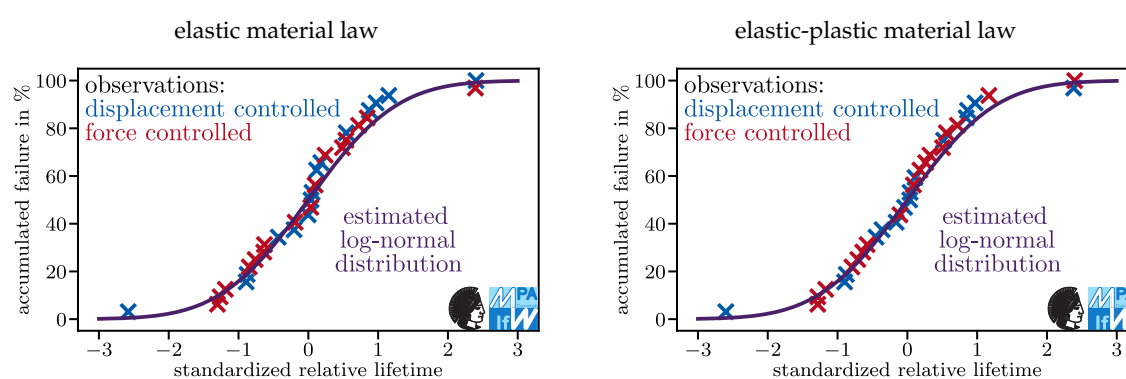
Figure 19. Estimated and observed accumulated failure rates for 50CrMo4 specimens in laboratory air; 1726 MPa ultimate tensile strength; $K_t = 2.06$.

Curves describing the observed accumulated failure rate would run horizontally from each observed data point and jump to the next level just before the next observation. This explains the impression that the estimated log-normal distributions are biased towards higher standardized relative failure rates.

One-sided tendencies of failure events under displacement and force control towards earlier or later lifetimes reflect systematic differences between the results obtained on both experimental setups. Such tendencies are eminent in all non-corrected test results obtained on specimens that were quenched and tempered to ultimate tensile strength levels of 919 MPa.

Quantile-quantile plots are given in Figures 20 to 25. These figures show the same as Figures 14 to 19, just in a differently scaled coordinate system with switched axes in which the cumulative function of the log-normal distribution is the 45° line. Good compliance with this line means that the data is well described by a normal distribution. In each figure, the p-value of the corresponding Shapiro-Wilk test is given. Low values imply a rejection of the null hypothesis. The null hypothesis is that the data set under investigation follows a log-normal distribution. The power of Shapiro-Wilk tests is lower in data sets with fewer specimens than in data sets with more specimens.
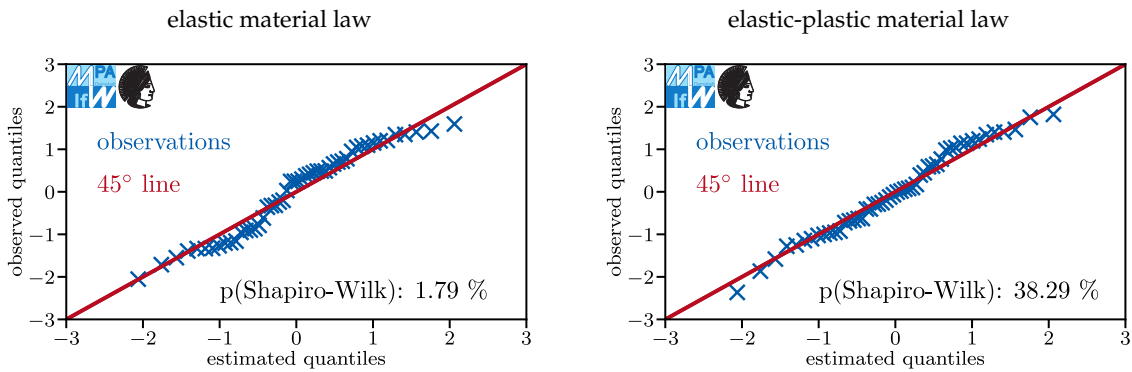
Figure 20. Quantile-quantile plots for 50CrMo4 specimens in laboratory air; 919 MPa ultimate tensile strength; $K_t = 1$.
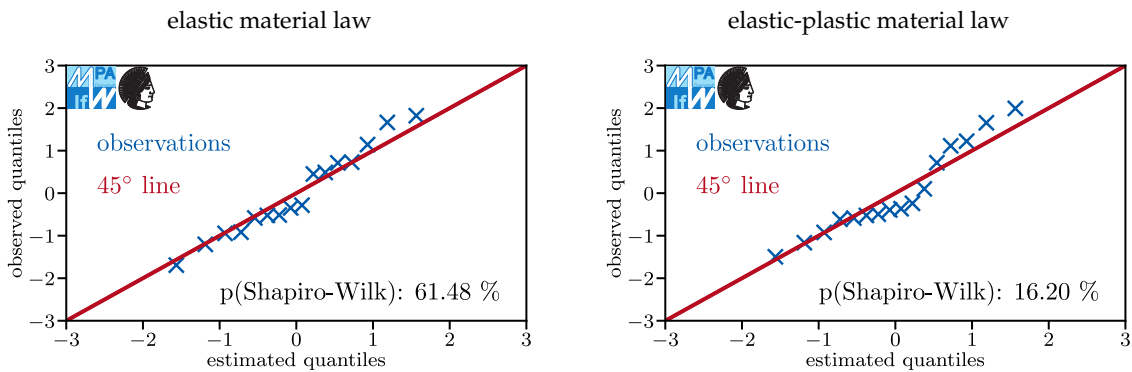
Figure 21. Quantile-quantile plots for 50CrMo4 specimens in laboratory air; 919 MPa ultimate tensile strength; $K_t = 1.75$.
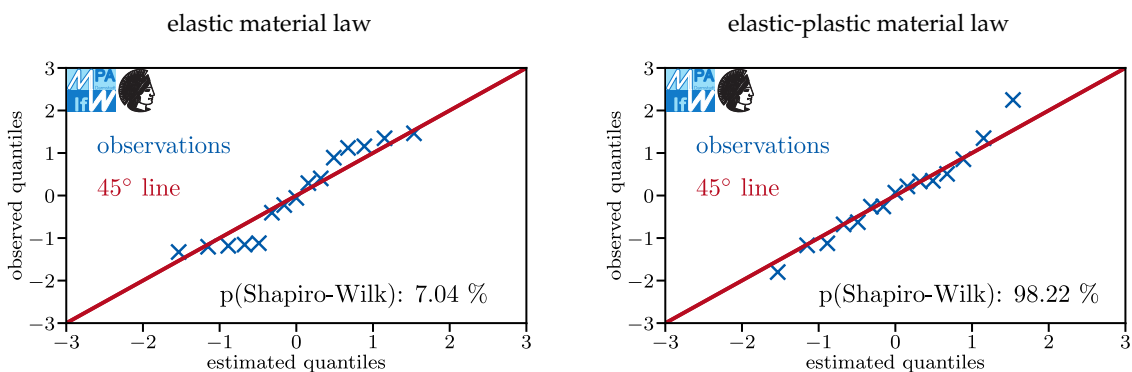
Figure 22. Quantile-quantile plots for 50CrMo4 specimens in argon; 919 MPa ultimate tensile strength; $K_t = 1.75$.
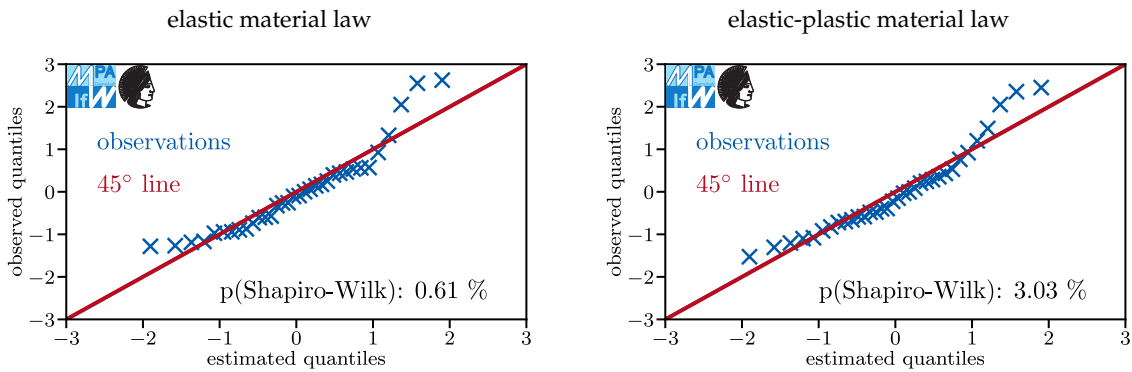
Figure 23. Quantile-quantile plots for 50CrMo4 specimens in laboratory air; 919 MPa ultimate tensile strength; $K_t = 2.06$.
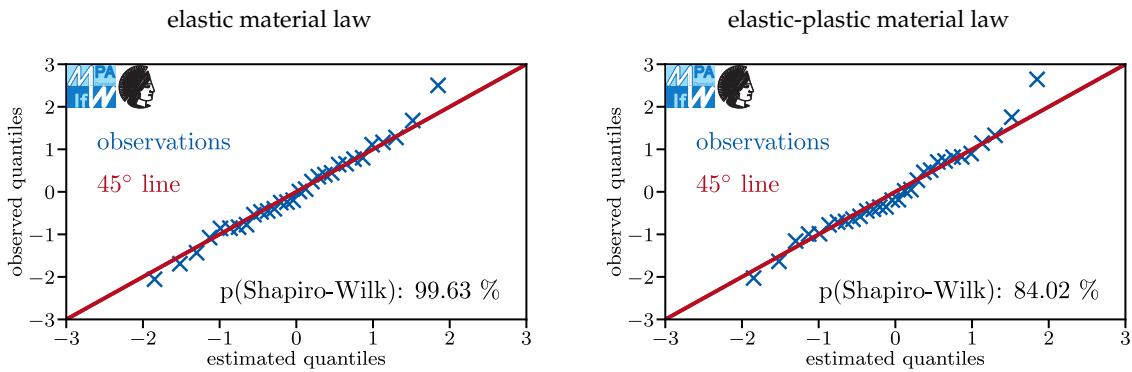
Figure 24. Quantile-quantile plots for 50CrMo4 specimens in laboratory air; 1096 MPa ultimate tensile strength; $K_t = 1.2$.
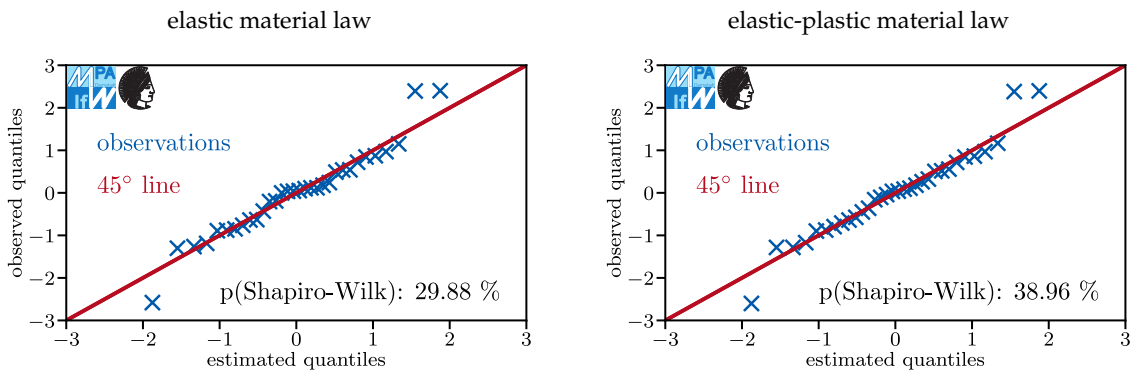
Figure 25. Quantile-quantile plots for 50CrMo4 specimens in laboratory air; 1726 MPa ultimate tensile strength; $K_t = 2.06$.

Although some systematic deviations are present, overall, the data sets agree with the models based on constant log-normal distributions, which implies that the assumption of a log-normal distribution is reasonable[8]. At a significance level of 5%, the Shapiro-Wilk test rejects normality for three out of twelve data sets.

---

8   This does not mean that the homoscedastic log-normal distribution is a good model overall. Actually, problems about model consistency and accordance to reality have been brought up in literature [30–35,100,144].

Author Contributions: Conceptualization, M.B.G.; methodology, M.B.G..; software, M.B.G., D.S.L. and J.A.S.; validation, M.B.G. and J.A.S.; formal analysis, M.B.G.; investigation, M.B.G. and M.K.; resources, M.O., M.K. and U.K.; data curation, M.B.G. and A.G.; writing–original draft preparation, M.B.G., M.K. and J.A.S.; writing–review and editing, M.B.G, J.A.S, M.K., D.S.L., A.G., U.K. and M.O.; visualization, M.B.G.; supervision, M.O.; project administration, M.K.; funding acquisition, M.O. All authors have read and agreed to the published version of the manuscript.

Funding: The authors thank the Federal Ministry of Economics and Technology, the German Federation of Industrial Research Associations 'Otto von Guericke' e.V. (BMWi/AiF no. 324ZN and AiF no. 18198 N) and the Forschungskuratorium Maschinenbau e.V. (FKM) for the financial support. We acknowledge support by the German Research Foundation and the Open Access Publishing Fund of Technical University Darmstadt.

Acknowledgments: Some of the data used in this paper was generated by Fraunhofer LBF in BMWi/AiF no. 324ZN and AiF no. 18198. We thank Dipl.-Ing. Klaus Störzel and Prof. Dr.-Ing Tobias Melz for the fruitful cooperation.

Conflicts of Interest: The authors declare no conflict of interest.

References

1. Dowling, N.E. *Mechanical behavior of materials: engineering methods for deformation, fracture, and fatigue*; Pearson, 2012.

2. Bathias, C. There is no infinite fatigue life in metallic materials. *Fatigue & Fracture of Engineering Materials & Structures* **1999**, *22*, 559–565.

3. Bathias, C.; Drouillac, L.; Le Francois, P. How and why the fatigue S-N curve does not approach a horizontal asymptote. *International Journal of Fatigue* **2001**, *23*, 143–151.

4. Schwerdt, D. *Schwingfestigkeit und Schädigungsmechanismen der Aluminiumlegierungen EN AW-6056 und EN AW-6082 sowie des Vergütungsstahls 42CrMo4 bei sehr hohen Schwingspielzahlen*; TU Darmstadt: Darmstadt, 2011.

5. Oechsner, M.; Hanselka, H.; Schneider, N.; Eufinger, J.; Pyttel, B.; Berger, C. *Schlussbericht zu BMWi 324 ZN: Bauteilauslegung unter Berücksichtigung von Beanspruchungen mit variablen Amplituden und sehr hohen Schwingspielzahlen*; MPA-IfW: Technische Universität Darmstadt, 2012.

6. Schneider, N. Ermüdungsfestigkeit bei sehr hohen Schwingspielzahlen unter Berücksichtigung des Einflusses der Prüffrequenz. Ph. D. Thesis, TU Darmstadt, Darmstadt, 2014.

7. Schneider, N.; Schwerdt, D.; Wuttke, U.; Oechsner, M. Fatigue at high number of cyclic loads: Testing methods and failure mechanism. *Materialwissenschaft und Werkstofftechnik* **2015**, *46*, 931–941.

8. Krupp, U.; Giertler, A.; Koschella, K. Microscopic Damage Evolution During Very High Cycle Fatigue (VHCF) of Tempered Martensitic Steel. *Procedia Engineering* **2016**, *160*, 231–238. doi:10.1016/j.proeng.2016.08.885.

9. Schneider, N.; Bödecker, J.; Berger, C.; Oechsner, M. Frequency effect and influence of testing technique on the fatigue behaviour of quenched and tempered steel and aluminium alloy. *International Journal of Fatigue* **2016**, *93*, 224–231.

10. Oechsner, M.; Melz, T.; Kaffenberger, M.; Störzel, K. AiF A 18198 N: Bauteilauslegung unter Berücksichtigung von Beanspruchungen mit variablen Amplituden und sehr hohen Schwingspielzahlen.

11. Mayer, H. Recent developments in ultrasonic fatigue. *Fatigue & Fracture of Engineering Materials & Structures* **2016**, *39*, 3–29.

12. Jeddi, D.; Palin-Luc, T. A review about the effects of structural and operational factors on the gigacycle fatigue of steels. *Fatigue & Fracture of Engineering Materials & Structures* **2018**, *41*, 969–990.

13. Kaiser, B.; Berger, C. Fatigue behaviour of technical springs. *Materialwissenschaft und Werkstofftechnik* **2005**, *36*, 685–696.

14. Berger, C.; Kaiser, B. *Schlussbericht zum IGF-Vorhaben Nr. 15064 N: Untersuchung der Dauerhubfestigkeit von Schraubenfedern im Bereich extrem hoher Schwingspielzahlen*; MPA-IfW: Technische Universität Darmstadt, 2010.

15. Kaiser, B.; Berger, C. Untersuchung der Dauerhubfestigkeit von Schraubenfedern im Bereich extrem hoher Schwingspielzahlen. Very high cycle fatigue behavior of helical compression springs. *Materialwissenschaft und Werkstofftechnik* **2010**, *41*, 829–838.

16. Kaiser, B.; Pyttel, B.; Berger, C. VHCF-behavior of helical compression springs made of different materials. *International Journal of Fatigue* **2011**, *33*, 23–32.

17. Oechsner, M.; Brunner, I. *Schlussbericht zum IGF-Vorhaben Nr. 16873 N: Untersuchung von Werkstoff- und Fertigungseinflüssen auf das VHCF-Verhalten von Schraubendruckfedern*; MPA-IfW: Technische Universität Darmstadt, 2014.

18. Pyttel, B.; Brunner, I.; Kaiser, B.; Berger, C.; Mahendran, M. Fatigue behaviour of helical compression springs at a very high number of cycles–Investigation of various influences. *International Journal of Fatigue* **2014**, *60*, 101–109.

19. Oechsner, M.; Brunner, I. *Schlussbericht zum IGF-Vorhaben Nr. 18576 N: Entwicklung einer standardisierten Auswertemethode zur betriebsfesten Auslegung von Schraubendruckfedern bei variabler Beanspruchung*; MPA-IfW: Technische Universität Darmstadt, 2017.

20. Geilen, M.B.; Klein, M.; Oechsner, M. Very high cycle fatigue behaviour of compression springs under constant and variable amplitude loading. *Materialwissenschaft und Werkstofftechnik* **2019**, *50*, 1301–1316.

21. Abe, T.; Furuya, Y.; Matsuoka, S. Gigacycle fatigue properties of 1800 MPa class spring steels. *Fatigue & Fracture of Engineering Materials & Structures* **2004**, *27*, 159–167. doi:10.1111/j.1460-2695.2004.00737.x.

22. Akiniwa, Y.; Stanzl-Tschegg, S.; Mayer, H.; Wakita, M.; Tanaka, K. Fatigue strength of spring steel under axial and torsional loading in the very high cycle regime. *International Journal of Fatigue* **2008**, *30*, 2057–2063.

23. Miura, T.; Sakai, T.; Sakakibara, T.; Mimura, S.; Kuno, T.; Kikuchi, S.; Ueno, A. Experimental investigation on effects of various factors on very high cycle fatigue property for spring steels. ICF13, 2013.

24. Mayer, H.; Schuller, R.; Karr, U.; Irrasch, D.; Fitzka, M.; Hahn, M.; Bacher-Höchst, M. Cyclic torsion very high cycle fatigue of VDSiCr spring steel at different load ratios. *International Journal of Fatigue* **2015**, *36*, 322–327.

25. Miura, T.; Sakakibara, T.; Kuno, T.; Ueno, A.; Kikuchi, S.; Sakai, T. Interior-induced fracture mechanism of high cleanliness spring steel (JIS SWOSC-V) in very high cycle regime. *Key Engineering Materials* **2015**, *664*, 209.

26. Mayer, H.; Schuller, R.; Karr, U.; Fitzka, M.; Irrasch, D.; Hahn, M.; Bacher-Höchst, M. Mean stress sensitivity and crack initiation mechanisms of spring steel for torsional and axial VHCF loading. *International Journal of Fatigue* **2016**, *93*, 309–317.

27. Karr, U.; Sandaiji, Y.; Tanegashima, R.; Murakami, S.; Schönbauer, B.; Fitzka, M.; Mayer, H. Inclusion initiated fracture in spring steel under axial and torsion very high cycle fatigue loading at different load ratios. *International Journal of Fatigue* **2020**, *134*, 105525.

28. Nishimura, Y.; Yanase, K.; Tanaka, Y.; Miyamoto, N.; Miyakawa, S.; Endo, M. Effects of mean shear stress on the torsional fatigue strength of a spring steel with small scratches. *International Journal of Damage Mechanics* **2020**, *29*, 4–18.

29. Pyttel, B.; Fernández Canteli, A.; Argente Ripoll, A. Comparison of different statistical models for description of fatigue including very high cycle fatigue. *International Journal of Fatigue* **2016**, *93*, 435–442.

30. Bomas, H.; Burkart, K.; Zoch, H.W. Evaluation of S–N curves with more than one failure mode. *International Journal of Fatigue* **2011**, *33*, 19–22.

31. Paolino, D.S.; Chiangdussi, G.; Rosetto, M. A unified statistical model for S–N fatigue curves: probabilistic definition. *Fatigue & Fracture of Engineering Materials & Structures* **2013**, *36*, 187–201. doi:10.1111/j.1460-2695.2012.01711.x.

32. Haydn, W.; Schwabe, F. Ermittlung geschlossener probabilistischer Auslegungskennlinien für einstufige Schwingfestigkeitsbeanspruchungen vom LCF- bis VHCF-Bereich. *Materialwissenschaft und Werkstofftechnik* **2015**, *46*, 591–602.

33. Fernández-Canteli, A.; Blasón, S.; Pyttel, B.; Muniz-Calvente, M.; Castillo, E. Considerations about the existence or non-existence of the fatigue limit: implications on practical design. *International Journal of Fracture* **2020**, pp. 1–8.

34. Muniz-Calvente, M.; Fernández-Canteli, A.; Pyttel, B.; Castillo, E. Probabilistic assessment of VHCF data as pertaining to concurrent populations using a Weibull regression model. *Fatigue & Fracture of Engineering Materials & Structures* **2017**, *40*, 1772–1782.

35. Kobelev, V. A proposal for unification of fatigue crack growth, 2018.

36. Bach, J. Ermüdungsverhalten von niedrig legierten Stählen im HCF-und VHCF-Bereich. Ph. D. thesis, Friedrich-Alexander-Universität Erlangen-Nürnberg, Erlangen, 2018.

37. Bach, J.; Göken, M.; Höppel, H.W. Fatigue of low alloyed carbon steels in the HCF/VHCF-regimes. In *Fatigue of Materials at Very High Numbers of Loading Cycles*; Springer, 2018; pp. 1–23.

38. Cai, Y.; Zhao, Y.; Ma, X.; Yang, Z.; Ding, Y. An extended model for fatigue life prediction and acceleration considering load frequency effect. *IEEE Access* **2018**, *6*, 21064–21074.

39. Hu, Y.; Sun, C.; Xie, J.; Hong, Y. Effects of loading frequency and loading type on high-cycle and very-high-cycle fatigue of a high-strength steel. *Materials* **2018**, *11*, 1456.

40. Geilen, M.B.; Klein, M.; Oechsner, M.; Kaffenberger, M.; Störzel, K.; Melz, T. A Method for the Strain Rate Dependent Correction for Control Type of Fatigue Tests. *International Journal of Fatigue* **2020**, p. 105726. doi:10.1016/j.ijfatigue.2020.105726.

41. Atrens, A.; Hoffelner, W.; Duerig, T.W.; Allison, J.E. Subsurface crack initiation in high cycle fatigue in Ti6A14V and in a typical martensitic stainless steel. *Scripta Metallurgica* **1983**, *17*, 601–606.

42. Furuya, Y.; Matsuoka, S.; Abe, T.; Yamaguchi, K. Gigacycle fatigue properties for high-strength low-alloy steel at 100 Hz, 600 Hz, and 20 kHz. *Scripta Materialia* **2002**, *46*, 157–162.

43. Furuya, Y.; Matsuoka, S. Gigacycle fatigue properties of a modified-ausformed Si-Mn steel and effects of microstructure. *Metallurgical and Materials Transactions A* **2004**, *35*, 1715–1723.

44. Tsutsumi, N.; Murakami, Y.; Doquet, V. Effect of test frequency on fatigue strength of low carbon steel. *Fatigue & Fracture of Engineering Materials & Structures* **2009**, *32*, 473–483.

45. Müller-Bollenhagen, C.; Zimmermann, M.; Christ, H.J. Adjusting the very high cycle fatigue properties of a metastable austenitic stainless steel by means of the martensite content. *Procedia Engineering* **2010**, *2*, 1663–1672.

46. Pyttel, B.; Schwerdt, D.; Berger, C. Fatigue strength and failure mechanisms in the VHCF-region for quenched and tempered steel 42CrMoS4 and consequences to fatigue design. *Procedia Engineering* **2010**, *2*, 1327–1336.

47. Setowaki, S.; Ichikawa, Y.; Nonaka, I. Effect of frequency on high cycle fatigue strength of railway axle steel. Proceedings of fifth International Conference on Very High Cycle Fatigue, VHCF5, 2011, pp. 153–158.

48. Nonaka, I.; Setowaki, S.; Ichikawa, Y. Effect of load frequency on high cycle fatigue strength of bullet train axle steel. *International Journal of Fatigue* **2014**, *60*, 43–47.

49. Guennec, B.; Ueno, A.; Sakai, T.; Takanashi, M.; Itabashi, Y. Effect of the loading frequency on fatigue properties of JIS S15C low carbon steel and some discussions based on micro-plasticity behavior. *International Journal of Fatigue* **2014**, *66*, 29–38.

50. Zhu, M.L.; Liu, L.L.; Xuan, F.Z. Effect of frequency on very high cycle fatigue behavior of a low strength Cr–Ni–Mo–V steel welded joint. *International Journal of Fatigue* **2015**, *77*, 166–173.

51. Torabian, N.; Favier, V.; Dirrenberger, J.; Adamski, F.; Ziaei-Rad, S.; Ranc, N. Correlation of the high and very high cycle fatigue response of ferrite based steels with strain rate-temperature conditions. *Acta Materialia* **2017**, *134*, 40–52.

52. Mayer, H.; Papakyriacou, M.; Pippan, R.; Stanzl-Tschegg, S. Influence of loading frequency on the high cycle fatigue properties of AlZnMgCu1. 5 aluminium alloy. *Materials Science and Engineering: A* **2001**, *314*, 48–54.

53. Papakyriacou, M.; Mayer, H.; Pypen, C.; Plenk Jr, H.; Stanzl-Tschegg, S. Influence of loading frequency on high cycle fatigue properties of bcc and hcp metals. *Materials Science and Engineering: A* **2001**, *308*, 143–152.

54. Mayer, H.; Ede, C.; Allison, J.E. Influence of cyclic loads below endurance limit or threshold stress intensity on fatigue damage in cast aluminium alloy 319-T7. *International Journal of Fatigue* **2005**, *27*, 129–141.

55. Engler-Pinto Jr, C.C.; Frisch Sr, R.J.; Lasecki, J.V.; Mayer, H.; Allison, J.E. Effect of frequency and environment on high cycle fatigue of cast aluminum alloys. In *VHCF-4*; 2007; pp. 421–427.

56. Takeuchi, E.; Furuya, Y.; Nagashima, N.; Matsuoka, S. The effect of frequency on the giga–cycle fatigue properties of a Ti–6Al–4V alloy. *Fatigue & Fracture of Engineering Materials & Structures* **2008**, *31*, 599–605.

57. Zhu, X.; Jones, J.W.; Allison, J.E. Effect of frequency, environment, and temperature on fatigue behavior of E319 cast aluminum alloy: stress-controlled fatigue life response. *Metallurgical and Materials Transactions A* **2008**, *39*, 2681–2688.

58. Begum, S.; Chen, D.L.; Xu, S.; Luo, A.A. Effect of strain ratio and strain rate on low cycle fatigue behavior of AZ31 wrought magnesium alloy. *Materials Science and Engineering: A* **2009**, *517*, 334–343.

59. Protz, R.; Kosmann, N.; Gude, M.; Hufenbach, W.; Schulte, K.; Fiedler, B. Voids and their effect on the strain rate dependent material properties and fatigue behaviour of non-crimp fabric composites materials. *Composites Part B: Engineering* **2015**, *83*, 346–351.

60. Jost, B.; Klein, M.; Beck, T.; Eifler, D. Temperature dependent cyclic deformation and fatigue life of EN-GJS-600 (ASTM 80-55-06) ductile cast iron. *International Journal of Fatigue* **2017**, *96*, 102–113.

61. Jost, B.; Klein, M.; Beck, T.; Eifler, D. Temperature and frequency influence on the cyclic deformation behavior of EN-GJS-600 (ASTM 80-55-06) ductile cast iron at 0.005 and 5 Hz. *International Journal of Fatigue* **2018**, *110*, 225–237.

62. Wang, M.; Pang, J.C.; Liu, H.Q.; Zou, C.L.; Li, S.X.; Zhang, Z.F. Deformation mechanism and fatigue life of an Al-12Si alloy at different temperatures and strain rates. *International Journal of Fatigue* **2019**, *127*, 268–274.

63. Campbell, J.D.; Ferguson, W.G. The temperature and strain-rate dependence of the shear strength of mild steel. *Philosophical Magazine* **1970**, *21*, 63–82.

64. Jaske, C.E.; Leis, B.N.; Pugh, C.E. Monotonic and cyclic stress-strain response of annealed 2 1/4 Cr–1 Mo steel.

65. El-Magd, E. Influence of strain rate on ductility of metallic materials. *Steel Research* **1997**, *68*, 67–71.

66. Bleck, W.; Schael, I. Determination of crash–relevant material parameters by dynamic tensile tests. *Steel Research* **2000**, *71*, 173–178.

67. Børvik, T.; Hopperstad, O.S.; Berstad, T. On the influence of stress triaxiality and strain rate on the behaviour of a structural steel. Part II. Numerical study. *European Journal of Mechanics-A/Solids* **2003**, *22*, 15–32.

68. Hopperstad, O.S.; Børvik, T.; Langseth, M.; Labibes, K.; Albertini, C. On the influence of stress triaxiality and strain rate on the behaviour of a structural steel. Part I. Experiments. *European Journal of Mechanics-A/Solids* **2003**, *22*, 1–13.

69. Lee, W.S.; Liu, C.Y. The effects of temperature and strain rate on the dynamic flow behaviour of different steels. *Materials Science and Engineering: A* **2006**, *426*, 101–113.

70. FAT-Richtlinie. Dynamische Werkstoffkennwerte für die Crashsimulation.

71. Emde, T. *Mechanisches Verhalten metallischer Werkstoffe über weite Bereiche der Dehnung, der Dehnrate und der Temperatur*; Verlagshaus Mainz GmbH: Aachen, 2009.

72. Benson, D.K.; Hancock, J.R. The effect of strain rate on the cyclic response of metals. *Metallurgical Transactions* **1974**, *5*, 1711–1715.

73. Pineau, A.; Benzerga, A.A.; Pardoen, T. Failure of metals I: Brittle and ductile fracture. *Acta Materialia* **2016**, *107*, 424–483.

74. Hodowany, J.; Ravichandran, G.; Rosakis, A.J.; Rosakis, P. Partition of plastic work into heat and stored energy in metals. *Experimental Mechanics* **2000**, *40*, 113–123.

75. Cho, K.M.; Lee, S.; Nutt.; Duffy, J. Adiabatic shear band formation during dynamic torsional deformation of an HY-100 steel. *Acta Metallurgica et Materialia* **1993**, *41*, 923–932.

76. Kapoor, R.; Nemat-Nasser, S. Determination of temperature rise during high strain rate deformation. *Mechanics of Materials* **1998**, *27*, 1–12.

77. Rosakis, P.; Rosakis, A.J.; Ravichandran, G.; Hodowany, J. A thermodynamic internal variable model for the partition of plastic work into heat and stored energy in metals. *Journal of the Mechanics and Physics of Solids* **2000**, *48*, 581–607.

78. Holzer, A.J.; Brown, R.H. Mechanical behavior of metals in dynamic compression. *0094-4289* **1979**.

79. Klepaczko. An experimental technique for shear testing at high and very high strain rates. The case of a mild steel. *International Journal of Impact Engineering* **1994**, *15*, 25–39.

80. Johnson, G.R.; Cook, W.H. Fracture characteristics of three metals subjected to various strains, strain rates, temperatures and pressures. *Engineering Fracture Mechanics* **1985**, *21*, 31–48.

81. Zerbst, U.; Vormwald, M.; Pippan, R.; Gänser, H.P.; Sarrazin-Baudoux, C.; Madia, M. About the fatigue crack propagation threshold of metals as a design criterion–a review. *Engineering Fracture Mechanics* **2016**, *153*, 190–243.

82. Tanaka, H.; Homma, N.; Matsuoka, S.; Murakami, Y. Effect of hydrogen and frequency on fatigue behavior of SCM435 steel for storage cylinder of hydrogen station. *Nihon Kikai Gakkai Ronbunshu, A Hen/Transactions of the Japan Society of Mechanical Engineers, Part A* **2007**, *73*, 1358–1365.

83. Murakami, Y.; Matsuoka, S. Effect of hydrogen on fatigue crack growth of metals. *Engineering Fracture Mechanics* **2010**, *77*, 1926–1940.

84. Suresh, S.; Ritchie, R.O. Near-threshold fatigue crack propagation: a perspective on the role of crack closure. In *Fatigue Crack Growth Threshold Concepts*; 1983.

85. Blom, A.F.; Holm, D.K. An experimental and numerical study of crack closure. *Engineering Fracture Mechanics* **1985**, *22*, 997–1011.

86. Vasudeven, A.K.; Sadananda, K.; Louat, N. A review of crack closure, fatigue crack threshold and related phenomena. *Materials Science and Engineering: A* **1994**, *188*, 1–22.

87. Chermahini, R.G.; Shivakumar, K.N.; Newman Jr, J.C.; Blom, A.F. Three-dimensional aspects of plasticity-induced fatigue crack closure. *Engineering Fracture Mechanics* **1989**, *34*, 393–401.

88. Pippan, R.; Hohenwarter, A. Fatigue crack closure: a review of the physical phenomena. *Fatigue & Fracture of Engineering Materials & Structures* **2017**, *40*, 471–495.

89. Jiang, Y.; Feng, M.; Ding, F. A reexamination of plasticity-induced crack closure in fatigue crack propagation. *International Journal of Plasticity* **2005**, *21*, 1720–1740.

90. Weibull, W. A statistical theory of strength of materials **1939**.

91. Kuhn, P. Effect of geometric size on notch fatigue. In *Colloquium on Fatigue 1956*; pp. 131–140.

92. Böhm, J.; Heckel, K. Die Vorhersage der Dauerschwingfestigkeit unter Berücksichtigung des statistischen Größeneinflusses. *Materialwissenschaft und Werkstofftechnik* **1982**, *13*, 120–128.

93. Liu, J.; Zenner, H. Berechnung der Dauerschwingfestigkeit unter Berücksichtigung der spannungsmechanischen und statistischen Stützziffer. *Materialwissenschaft und Werkstofftechnik* **1991**, *22*, 187–196.

94. Liu, J.; Zenner, H. Berechnung von Bauteilwöhlerlinien unter Berücksichtigung der statistischen und spannungsmechanischen Stützziffer. *Materialwissenschaft und Werkstofftechnik* **1995**, *26*, 14–21.

95. Kloos, K.H.; Kaiser, B.; Friederich, H. Einfluß der Probengröße auf das Verformungs–und Versagensverhalten von Vergütungsstahl 42 CrMo 4 unter Schwingbeanspruchung. *Materialwissenschaft und Werkstofftechnik* **1995**, *26*, 330–336.

96. Friederich, H.; Kaiser, B.; Kloos, K.H. Anwendung der Fehlstellentheorie nach Weibull zur Berechnung des statistischen Größeneinflusses bei Dauerschwingbeanspruchung. *Materialwissenschaft und Werkstofftechnik* **1998**, *29*, 178–184.

97. Bomas, H.; Linkewitz, T.; Mayr, P. Application of a weakest–link concept to the fatigue limit of the bearing steel SAE 52100 in a bainitic condition. *Fatigue & Fracture of Engineering Materials & Structures* **1999**, *22*, 733–741.

98. Makkonen, M. Statistical size effect in the fatigue limit of steel. *International Journal of Fatigue* **2001**, *23*, 395–402.

99. Flacelière, L.; Morel, F. Probabilistic approach in high–cycle multiaxial fatigue: volume and surface effects. *Fatigue & Fracture of Engineering Materials & Structures* **2004**, *27*, 1123–1135.

100. Castillo, E.; Fernandez-Canteli, A. *A unified statistical methodology for modeling fatigue damage*; Springer Science & Business Media, 2009.

101. Hertel, O.; Vormwald, M. Statistical and geometrical size effects in notched members based on weakest-link and short-crack modelling. *Engineering Fracture Mechanics* **2012**, *95*, 72–83.

102. Ai, Y.; Zhu, S.P.; Liao, D.; Correia, J.A.; de Jesus, A.M.P.; Keshtegar, B. Probabilistic modelling of notch fatigue and size effect of components using highly stressed volume approach. *International Journal of Fatigue* **2019**, *127*, 110–119.

103. Vaara, J.; Väntänen, M.; Kämäräinen, P.; Kemppainen, J.; Frondelius, T. Bayesian analysis of critical fatigue failure sources. *International Journal of Fatigue* **2020**, *130*, 105282.

104. Rennert, R.; Kullig, E.; Vormwald, M.; Esderts, A.; Siegele, D. *Rechnerischer Festigkeitsnachweis für Maschinenbauteile aus Stahl, Eisenguss- und Aluminiumwerkstoffen*, 6 ed.; FKM-Richtlinie, VDMA Verlag: Frankfurt am Main, 2012.

105. Fiedler, M.; Wächter, M.; Varfolomeev, I., Vormwald, M..; Esderts, A. *Rechnerischer Festigkeitsnachweis unter expliziter Erfassung nichtlinearen Werkstoffverhaltens für Maschinenbauteile aus Stahl, Stahlguss und Aluminiumknetlöegierungen*, 1 ed.; FKM-Richtlinie, VDMA Verlag: Frankfurt am Main, 19.

106. Kletzin, U.; Reich, R.; Oechsner, M.; Spies, A.; Pyttel, B.; Hanning, G.; Rennert, R.; Kullig, E. *Rechnerischer Festigkeitsnachweis für Federn und Federelemente*, 1 ed.; FKM-Richtlinie, VDMA Verlag: Frankfurt am Main, 2020.

107. Skelton, R.P.; Haigh. Fatigue crack growth rates and thresholds in steels under oxidising conditions. *Materials Science and Engineering* **1978**, *36*, 17–25.

108. Suresh, S.; Zamiski, G.F.; Ritchie, D.R.O. Oxide-induced crack closure: an explanation for near-threshold corrosion fatigue crack growth behavior. *Metallurgical and Materials Transactions A* **1981**, *12*, 1435–1443.

109. Liaw, P.K.; Leax, T.R.; Williams, R.S.; Peck, M.G. Influence of oxide-induced crack closure on near-threshold fatigue crack growth behavior. *Acta Metallurgica* **1982**, *30*, 2071–2078.

110. Maierhofer, J.; Simunek, D.; Gänser, H.P.; Pippan, R. Oxide induced crack closure in the near threshold regime: The effect of oxide debris release. *International Journal of Fatigue* **2018**, *117*, 21–26.

111. Riemelmoser, F.O.; Gumbsch, P.; Pippan, R. Dislocation modelling of fatigue cracks: an overview. *Materials Transactions* **2001**, *42*, 2–13.

112. Lee, H.H.; Uhlig, H.H. Corrosion fatigue of type 4140 high strength steel. *Metallurgical and Materials Transactions B* **1972**, *3*, 2949–2957.

113. Shives, T.R.; Bennett, J.A. The Effect of Environment on the Fatigue Strengths of Four Selected Alloys.

114. Wadsworth, N.J. The influence of atmospheric corrosion on the fatigue limit of iron-0.5% carbon. *Philosophical Magazine* **1961**, *6*, 397–401.

115. Yoshinaka, F.; Nakamura, T. Effect of vacuum environment on fatigue fracture surfaces of high strength steel. *Mechanical Engineering Letters* **2016**, *2*, 15–00730.

116. Spriestersbach, D. VHCF-Verhalten des hochfesten Stahls 100Cr6: Rissinitiierungsmechanismen und Schwellenwerte. Ph. D. Thesis, TU Kaiserslautern, Kaiserslautern, 2020.

117. Wei, R.; Talda, P.; Li, C.Y. Fatigue-crack propagation in some ultrahigh-strength steels. In *Fatigue Crack Propagation*; ASTM International, 1967.

118. Dahlberg, E.P. Fatigue-crack propagation in high-strength 4340 steel in humid air(Water vapor effects on fatigue crack propagation rates in high strength 4340 steel examined by optical and electron fractography). *ASM Transactions Quarterly* **1965**, *58*, 46–53.

119. Achter, M. Effect of environment on fatigue cracks. In *Fatigue Crack Propagation*; ASTM International, 1967.

120. Henaff, G.; Marchal, K.; Petit, J. On fatigue crack propagation enhancement by a gaseous atmosphere: experimental and theoretical aspects. *Acta Metallurgica et Materialia* **1995**, *43*, 2931–2942.

121. Spriestersbach, D.; Grad, P.; Brodyanski, A.; Lösch, J.; Kopnarski, M.; Kerscher, E. Very high cycle fatigue crack initiation: investigation of fatigue mechanisms and threshold values for 100Cr6. In *Fatigue of Materials at Very High Numbers of Loading Cycles*; Springer, 2018; pp. 167–210.

122. Thompson, N.; Wadsworth, N.J.; Louat, N. The origin of fatigue fracture in copper. *Philosophical Magazine* **1956**, *1*, 113–126.

123. Duquette, D.J. Environmental Effects on General Fatigue Resistance and Crack Nucleation in Metals and Alloys.

124. Hudson, C.M.; Seward, S.K. A literature review and inventory of the effects of environment on the fatigue behavior of metals. *Engineering Fracture Mechanics* **1976**, *8*, 315–329.

125. Krupp, U. Mikrostrukturelle Aspekte der Rissinitiierung und-ausbreitung in metallischen Werkstoffen. Habilitation, Universität Siegen, Siegen, 2004.

126. Bradhurst, D.H.; Leach, J.L. The mechanical properties of thin anodic films on aluminum. *Journal of the Electrochemical Society* **1966**, *113*, 1245.

127. Grosskreutz, J.C. The effect of oxide films on dislocation-surface interactions in aluminum. *Surface Science* **1967**, *8*, 173–190.

128. Nakamura, T.; Oguma, H.; Shinohara, Y. The effect of vacuum-like environment inside sub-surface fatigue crack on the formation of ODA fracture surface in high strength steel. *Procedia Engineering* **2010**, *2*, 2121–2129.

129. Petit, J.; Sarrazin-Baudoux, C. An overview on the influence of the atmosphere environment on ultra-high-cycle fatigue and ultra-slow fatigue crack propagation. *International Journal of Fatigue* **2006**, *28*, 1471–1478.

130. Murakami, Y.; Nomoto, T.; Ueda, T.; Murakami, Y. On the mechanism of fatigue failure in the superlong life regime (N> 10000000 cycles). Part 1: influence of hydrogen trapped by inclusions. *Fatigue & Fracture of Engineering Materials & Structures* **2000**, *23*, 893–902.

131. Murakami, Y.; Nomoto, T.; Ueda, T.; Murakami, Y. On the mechanism of fatigue failure in the superlong life regime (N> 10000000 cycles). Part II: influence of hydrogen trapped by inclusions. *Fatigue & Fracture of Engineering Materials & Structures* **2000**, *23*, 903–910.

132. Barrera, O.; Tarleton, E.; Tang, H.W.; Cocks, A.C. Modelling the coupling between hydrogen diffusion and the mechanical behaviour of metals. *Computational Materials Science* **2016**, *122*, 219–228.

133. Barrera, O.; Bombac, D.; Chen, Y.; Daff, T.D.; Galindo-Nava, E.; Gong, P.; Haley, D.; Horton, R.; Katzarov, I.; Kermode. Understanding and mitigating hydrogen embrittlement of steels: a review of experimental, modelling and design progress from atomistic to continuum. *Journal of Materials Science* **2018**, *53*, 6251–6290.

134. Giertler, A. *Mechanismen der Rissentstehung und -ausbreitung im Vergütungsstahl 50CrMo4 bei sehr hohen Lastspielzahlen*, [1. auflage] ed.; Vol. 2020, Band 2, *Berichte aus dem Institut für Eisenhüttenkunde*, Shaker Verlag: Düren, 2020.

135. Ramberg, W.; Osgood, W.R. Description of stress-strain curves by three parameters.

136. Neuber, H. Über die Berücksichtigung der Spannungskonzenlration bei Festigkeitsproblemen. *Konstruktion, Berlin* **1968**, *1*.

137. Topper, T.; Wetzel, R.M.; Morrow, J. Neuber's rule applied to fatigue of notched specimens.

138. Wächter, M. *Zur Ermittlung von zyklischen Werkstoffkennwerten und Schädigungsparameterwöhlerlinien*; Technische Universität Clausthal, 2016.

139. Müller, C. *Zur statistischen Auswertung experimenteller Wöhlerlinien*; Universitätsbibliothek Clausthal, 2015.

140. Müller, C.; Wächter, M.; Masendorf, R.; Esderts, A. Distribution functions for the linear region of the SN curve. *Materials Testing* **2017**, *59*, 625–629.

141. Radaj, D.; Vormwald, M. *Ermüdungsfestigkeit*; Springer, 2007.

142. Glaser, A. *Mittelspannungseinfluß auf das Verformungsverhalten von Ck 45 und 42 CrMo 4 bei spannungs-und dehnungskontrollierter homogen-einachsiger Schwingbeanspruchung*; na, 1988.

143. Virtanen, P.; Gommers, R.; Oliphant, T.E.; Haberland, M.; Reddy, T.; Cournapeau, D.; Burovski, E.; Peterson, P.; Weckesser, W.; Bright, J. SciPy 1.0–Fundamental Algorithms for Scientific Computing in Python. *arXiv preprint arXiv:1907.10121* **2019**.

144. Geilen, M.B.; Klein, M.; Oechsner, M. On the Influence of Ultimate Number of Cycles on Lifetime Prediction for Compression Springs Manufactured from VDSiCr Class Spring Wire. *Materials* **2020**, *13*, 3222.